THE ASTROPHYSICAL JOURNAL, 364:370–395, 1990 December 1

POTENTIAL, VELOCITY, AND DENSITY FIELDS FROM REDSHIFT-DISTANCE SAMPLES: APPLICATION: COSMOGRAPHY WITHIN 6000 KILOMETERS PER SECOND

EDMUND BERTSCHINGER[1]
Department of Physics, Massachusetts Institute of Technology
AVISHAI DEKEL
Racah Institute of Physics, The Hebrew University of Jerusalem
S. M. FABER
UCO/Lick Observatory and Board of Studies in Astronomy and Astrophysics, University of California, Santa Cruz
ALAN DRESSLER
The Observatories of The Carnegie Institution of Washington
AND
DAVID BURSTEIN
Department of Physics, Arizona State University
Received 1989 December 28; accepted 1990 May 30

ABSTRACT

We present the first results of applying a potential flow reconstruction algorithm to the real universe. The method, described in detail in the preceding paper, takes as input radial peculiar velocities and distances for a set of objects that trace large-scale motions. Our sample is based on 544 early-type galaxies with $D_n - \sigma$ distance estimates and 429 spirals with infrared Tully-Fisher distances. From these data, the method reconstructs the three-dimensional potential, velocity, and mass density fields smoothed on large scales. The results are shown as maps of these fields, revealing the three-dimensional structure within 6000 km s^{-1} distance from the Local Group. For each map we provide an error map based on Monte Carlo simulations.

The dominant recovered structure is an extended, deep potential well in the Hydra-Centaurus region, stretching across the Galactic plane toward Pavo, broadly confirming the "great attractor" (GA) model of Lynden-Bell *et al.* (1988). The peak density contrast in this region is given by $\Omega^{4/7}\delta\rho/\rho = 1.2 \pm 0.4$ with a Gaussian smoothing window of radius ≈ 1400 km s^{-1}. The Local Supercluster appears to be an extended ridge on the near flank of the GA, proceeding through the Virgo Southern Extension to the Virgo and Ursa Major clusters. The Virgo cluster and the Local Group are both falling toward the bottom of the GA potential well, with peculiar velocities (smoothed on a scale of 500 km s^{-1}) of 658 ± 121 km s^{-1} and 565 ± 125 km s^{-1}, respectively. Several large regions of below-average mass density are discovered that match known voids in the galaxy distribution. A general correlation exists between the mass and galaxy distributions, except for a significant disagreement in the Perseus-Pisces supercluster, which is practically invisible in the reconstructed mass distribution. However, the very sparse sampling of measured distances in the current sample may cause us to underestimate the amplitude of both positive and negative density perturbations in that direction. The average velocities in spheres of radii 4000 and 6000 km s^{-1} centered on the Local Group (with prior, additional smoothing by a Gaussian of radius 1200 km s^{-1}) are 388 ± 67 km s^{-1} toward $L = 177°$, $B = -15°$, and 327 ± 82 km s^{-1} toward $L = 194°$, $B = 5°$, respectively, compared with predicted rms velocities of 287 and 224 km s^{-1} for the unbiased cold dark matter model.

Subject headings: cosmology — dark matter — galaxies: clustering — galaxies: formation

I. INTRODUCTION

Mapping the large-scale structure of the universe has, until recently, been accomplished exclusively with galaxy redshift surveys, with redshift providing a measure of distance through the Hubble law. Redshift surveys provide an efficient way to explore the galaxy distribution in large volumes, but they have two major limitations. First, redshifts do not give the true distances because of peculiar velocities, so that physical structures become displaced and distorted when viewed in redshift space. Second, galaxies are not necessarily faithful tracers of the total mass distribution. Dark matter probably exists far away from galaxies, with galaxy formation possibly biased toward certain regions due to uncertain physical processes (see Dekel and Rees 1987 for a review of biased galaxy formation). Because of these two limitations, comparison of redshift surveys with theoretical models is not straightforward.

Peculiar velocity measurements, obtained from redshifts and independently measured distances, can solve both of the problems facing redshift surveys, yielding results that are easier to compare with theories. If gravity is responsible for the deviations from perfect Hubble flow—and this is a fundamental postulate of nearly all theories of large-scale structure—then the peculiar velocity field is related on large scales in a direct way to the mass density field. Redshift-distance surveys may therefore provide the best undistorted map of the large-scale total (dark and luminous) mass distribution.

The first attempts to interpret redshift-distance data involved fitting simple three-dimensional flow models with a few free parameters to the measured pattern of radial peculiar

[1] Alfred P. Sloan Foundation Fellow.

velocities. This technique was pioneered by Rubin and colleagues (Rubin, Thonnard, and Ford 1976), who solved for the velocity of the Local Group (LG) relative to Sc galaxies in the redshift interval $3500 < cz < 6500$ km s^{-1}. Their result was interpreted as a systematic motion—a bulk flow—of distant galaxies with respect to the frame of the cosmic microwave background (CMB) radiation of some 850 km s^{-1}. This unexpectedly large value was at odds with all theoretical expectations and was challenged both by theorists (Fall and Jones 1976) and by other observers (Hart and Davies 1982; de Vaucouleurs and Peters 1984). However, Collins, Joseph, and Robertson (1986) reanalyzed the Rubin *et al.* sample using infrared photometry and confirmed the original findings.

All of the above measurements were based on distance indicators with relatively large statistical errors ($\gtrsim$25% relative error per galaxy). With the development of the more accurate infrared Tully-Fisher (IRTF) method for spiral galaxies (Tully and Fisher 1977; Aaronson, Huchra, and Mould 1979), Aaronson *et al.* (1986) measured the peculiar velocities of 10 distant clusters of spirals and found a much smaller large-scale motion, although their volume was not exactly comparable to that of Rubin *et al.*

On a smaller scale, the motions in our neighborhood have traditionally been modeled by a spherically symmetric inflow toward the Virgo cluster at the center of the Local Supercluster (LSC) (for a review, see Davis and Peebles 1983). For example, using a sample of 306 spiral galaxies with IRTF distances out to a redshift of about 3000 km s^{-1}, Aaronson *et al.* (1982*b*) obtained a best-fit LSC flow model with a total velocity of the Local Group (LG) toward Virgo of 331 $\pm$ 41 km s^{-1}, including a systematic spherical infall of 250 $\pm$ 64 km s^{-1}, and a rotation of the LSC with a magnitude of 180 $\pm$ 58 km s^{-1}, both evaluated at the distance of the LG from Virgo. The distance to Virgo was measured to be $\approx$1300 km s^{-1}, in the direction (L, B) = (103, -2). (We measure distances in km s^{-1} to avoid having to choose a value for the Hubble constant and use Supergalactic coordinates L, B in degrees or X, Y, Z [de Vaucouleurs, de Vaucouleurs, and Corwin 1975]).

The next major advance came with the analysis of a nearly magnitude-limited, all-sky survey of $\sim$400 elliptical galaxies out to a distance $\gtrsim$6000 km s^{-1} (Dressler *et al.* 1987*b*; Lynden-Bell *et al.* 1988). Dressler *et al.* (1987*a*) and Djorgovski and Davis (1987) discovered a new method for measuring accurate relative distances to ellipticals, termed the $D_n - \sigma$ method, which Dressler *et al.* (1987*b*) applied to their survey. The peculiar velocities of galaxies within 6000 km s^{-1} of the LG were modeled by a bulk motion in the CMB frame of 599 $\pm$ 104 km s^{-1} toward $L = 173°$, $B = -5°$. For comparison, the LG velocity in the CMB frame, based on the microwave background dipole, is $\sim$620 km s^{-1} toward (136, -38) (Lubin *et al.* 1985).

A more elaborate multiparameter model of the elliptical velocity field was developed by Lynden-Bell *et al.*, with the flow dominated by spherical infall into a "great attractor" (GA), an extended mass concentration centered at a distance $\approx$4200 km s^{-1} in the direction (161, -6) (using the updated fit of Faber and Burstein 1988). The GA includes the Hydra-Centaurus supercluster (Shaya 1984; Tammann and Sandage 1985; Lilje, Yahil, and Jones 1986) and lies close to the dust-obscured Galactic plane. (The Centaurus clusters are in the direction [156, -11]; Hydra is at [139, -37]; and NGC 3557 is at [150, -29]). In this model, the GA produces a peculiar velocity of magnitude 535 km s^{-1} at the distance of the LG. This large flow toward the GA is perturbed by a smaller spherical infall toward Virgo, of amplitude $\sim$100 km s^{-1} at the LG, plus a local "anomaly" of 360 km s^{-1} for the galaxies within a distance of 700 km s^{-1} from the LG (Lynden-Bell *et al.* 1988; Faber and Burstein 1988; see also Burstein 1990 and references therein).

Simple geometrical models like these are helpful in conveying an intuitive, qualitative picture of the large-scale motions. However, it is difficult to assess the theoretical implications of such *a posteriori*, multiparameter models (e.g., Bertschinger and Juszkiewicz 1988). For the best comparison with theories, one prefers a variety of simple *a priori* statistics related to the power spectrum of initial density fluctuations, such as the bulk flow in spheres of varying radii (Vittorio and Turner 1987; Kaiser 1988; Górski, Hoffman, and Bertschinger 1990), velocity correlation functions (Kaiser 1989; Górski *et al.* 1989; Groth, Juszkiewicz, and Ostriker 1989), or the cosmic Mach number (Ostriker and Suto 1989). Even these statistics, which in practice can be measured using only the radial component of peculiar velocity, do not provide a very clear representation of the peculiar velocity field. Their interpretation may require additional assumptions such as global isotropy. It would be far better to obtain and analyze the full three-dimensional velocity field, if it can be extracted from the data.

Another serious problem for theoretical modeling of large-scale motions is the fact that the peculiar velocity samples are *sparse* and *noisy*. Current samples contain $\sim$1000 galaxies with estimated distances out to $\sim$8000 km s^{-1}, and these are spread very nonuniformly throughout the volume. Within $\sim$2500 km s^{-1}, which is sampled fairly densely with IRTF measurements of spiral distances, the Galactic plane obscures a significant part of the volume. Even more problematic is the fact that each distance estimate carries a statistical error, of order 20% per galaxy, arising from the finite width of the distance indicator relations. Beyond 3000 km s^{-1}, the typical error exceeds the typical peculiar velocity ($\sim$600 km s^{-1}, based on the CMB dipole), although distance errors may be reduced by grouping galaxies in clusters.

We have developed a method for dealing with these problems, allowing us to recover from redshift-distance samples the full three-dimensional velocity field, as well as the mass density and potential fields, with control and evaluation of the effects of random distance errors. The method, which we have nicknamed POTENT, is described in detail in an associated paper (Dekel, Bertschinger, and Faber 1990; hereafter DBF). The main ideas of POTENT were introduced by Bertschinger and Dekel (1989; hereafter BD). A summary of the method is given by Bertschinger and Dekel (1990; hereafter BD90).

The key ideas of POTENT can be summarized as follows. Given the radial velocities u_i of a sparse sample of N galaxies with measured positions $\boldsymbol{r}_i$ and estimated distance measurement errors σ_i, we first smooth and interpolate the data using a tensor window function to produce a smoothed radial velocity field, $u(\boldsymbol{r})$, that can be evaluated at any desired point inside a spherical volume. The smoothing procedure yields the most likely value of the radial velocity averaged over a local spherical Gaussian window centered on $\boldsymbol{r}$. Then, in order to obtain the tangential components of the velocity field $\boldsymbol{v}(\boldsymbol{r})$, of which $u(\boldsymbol{r})$ is the radial component, we make the crucial assumption that the velocity field is derived from a scalar *potential*:

$$\boldsymbol{v}(\boldsymbol{r}) = -\nabla\Phi(\boldsymbol{r}) \,. \tag{1}$$

In other words, we assume that the peculiar velocity field is

irrotational, i.e., it has zero vorticity. According to the gravitational instability theory, this *velocity* potential is proportional to the *gravitational* potential in the linear regime and is related to it via the Bernoulli equation in the nonlinear regime (DBF). The velocity potential at each point on a spherical grid is calculated by integrating the radial component along radial rays,

$$\Phi(r) = -\int_0^r u(r', \theta, \phi)dr' . \quad (2)$$

Differentiating this potential in the transverse directions finally recovers the two missing components of the velocity.

We first demonstrated in BD that a potential flow analysis can be applied successfully to an idealized, smoothed cosmological N-body simulation, where the problems of sparse and noisy data were ignored. Then, in DBF, we showed how to deal with nonuniform spatial sampling and measurement errors. We tested the complete method by applying it to an N-body simulation using the actual "mask" of the positions of observed objects. The errors were analyzed carefully using both analytical and Monte Carlo techniques.

In this paper we present the first results obtained from applying POTENT to the real universe, based on the current data (§ II). Our intention is to convey a visual impression of the three-dimensional dynamics and cosmography in our local part of the universe. After summarizing our smoothing procedure (§ III), we present maps of the recovered potential, velocity, and density fields in nine slices cut from a sphere around us, plus maps of the estimated errors in these quantities (§ IV). Statistical analysis of the results and comparisons with the galaxy distribution and with theoretical scenarios are mentioned only briefly (§§ V, VI) as we will pursue these areas more thoroughly in future papers. Preliminary results are also discussed by Dekel and Bertschinger (1990; hereafter DB90).

II. THE DATA

Several studies have yielded large numbers of galaxies with measured distances. The distance indicators in these studies are based on galaxy scaling laws. For spirals, the infrared Tully-Fisher law is used, which relates rotation velocity to absolute H (or I) magnitude (e.g., Aaronson, Huchra and Mould 1979). For elliptical and S0 galaxies, the relevant law is the $D_n - \sigma$ relation, which relates velocity dispersion to a photometrically measured diameter (Dressler *et al.* 1987*a*; Djorgovski and Davis 1987; Dressler 1987; Faber *et al.* 1989). Even with perfect photometric and spectroscopic measurements, the estimated distances are only approximate because galaxies do not exactly obey the assumed scaling laws.

The raw ingredients for POTENT are a set of distances r_i and redshifts z_i (corrected to the CMB frame) for a set of N objects (galaxies or clusters) with directions given by the unit vectors $\hat{\mathbf{r}}_i$. The radial peculiar velocity is $u_i = cz_i - r_i$. Measurement errors in cz_i and $\hat{\mathbf{r}}_i$ are negligible, but errors in r_i are significant, and they translate directly into peculiar velocity errors. To minimize the variance in our smoothed velocity field, we weight each point inversely by the variance σ_i^2 of measured distance. Since distance errors increase linearly with distance, we set $\sigma_i = r_i\Delta$, with $\Delta = 0.16$ for spirals with IRTF distances and $\Delta = 0.21$ for ellipticals and S0s with $D_n - \sigma$ distances (Faber and Burstein 1988).

Besides having large random errors, distance measurements are subject to systematic errors, such as so-called Malmquist bias (Lynden-Bell *et al.* 1988; DBF). This bias results from the coupling of random distance measurement errors with the run of spatial density of objects along the line of sight. For a uniform space density of objects, the true distance r_i is on average higher than the raw estimated distance r_{ie} because the volume element grows as r^2; more galaxies are therefore scattered into each measurement volume from distant volumes than from nearer ones. The correction for uniform density is $r_i = r_{ie}(1 + 3.5\Delta^2)$. Since this bias affects all the raw distance measurements we use, we routinely apply this uniform-density correction to all the input data.

The Malmquist bias for clumpy distributions is more complicated and can be positive or negative depending on the radial density gradient. This bias is highly systematic—the distance errors are spatially correlated—and is not removed by smoothing unless the smoothing scale is considerably larger than the typical distance error. Since the bias is difficult to remove analytically, we have resorted to Monte Carlo simulations to distinguish real velocities from bias artifacts (DBF).

To minimize Malmquist bias, we have grouped galaxies into clusters of N_c points by adopting the group assignments of the original authors. The rms random distance error per object (galaxy or cluster) is then $r_i\Delta N_c^{-1/2}$, and the bias correction (for uniform density) is reduced by N_c^{-1} (Lynden-Bell *et al.* 1988).

The present data set was compiled from the sources listed in Table 1. Both spiral and elliptical surveys are represented. The principles used to select galaxies are quite different in the different sources, and only two surveys (Lynden-Bell *et al.* 1988 and Dressler and Faber 1990*a*) can claim to be magnitude-limited in their respective areas of sky. Even with a magnitude-limited survey, sampling efficiency declines drastically with distance. This fact, combined with the inhomogeneity of the galaxy distribution, leaves large volumes unsampled, requiring us to use a large smoothing length.

The data divide naturally into two subsets with different spatial scales and space densities. The backbone of the nearby data is the all-sky field spiral survey of Aaronson *et al.* (1982*a*, hereafter A82; also Bothun *et al.* 1984, hereafter B84), from which we used 211 galaxies with "good" distances (Faber and Burstein 1988). To this, 14 field galaxies were added from Aaronson *et al.* (1989, hereafter A89) to give a total of 225 field spirals. This sample gives a fairly dense and accurate sampling

TABLE 1

SOURCES OF DATA

References	Type of Galaxy and Region	Number[a]
1.....	Magnitude-limited survey of Es over whole sky	372
2.....	plus deeper E clusters	400
3.....	E/S0s in southern clusters	76
4.....	Magnitude-limited survey of E/S0s toward the GA	110
Total E/S0, including combinations of the above		544
5.....	Nearby field S's over whole sky	211
6.....	10 northern S clusters (minus Virgo and UMa)	148
7.....	7 southern S clusters plus 14 field galaxies	70
Total S		429

[a] Number of galaxies used here.

REFERENCES.—(1) Lynden-Bell *et al.* 1988, 7S; (2) Faber *et al.* 1989; (3) LC; (4) DF; (5) A82, B84; (6) A86; (7) A89.

of the velocity field within $\sim$2500 km s^{-1}, although even within this volume large regions are empty.

The backbone of the large-scale data is the all-sky elliptical survey by Lynden-Bell *et al.* (1988, 7S; Faber *et al.* 1989), which contains 145 individual galaxies plus 57 groups with more than one measured member. Ellipticals and S0s from new surveys of the GA region by Dressler and Faber (1990*a*, hereafter DF) and by Lucey and Carter (1988, hereafter LC) were merged and grouped with 7S to give 251 objects altogether. Duplicate observations of ellipticals and S0s have been averaged with equal weights. To the early-type galaxies, we add 17 spiral cluster distances: 10 in the Arecibo declination strip from Aaronson *et al.* (1986, hereafter A86; Virgo, Fornax, and Ursa Major are excluded as they are already contained in the A82 field sample) and seven from Aaronson *et al.* (1989, A89) in the GA region. The net result for the large-scale sample is a rather skeletal sampling of the whole volume out to $\sim$6000 km s^{-1} that is highly biased to high-density regions, plus a much more densely sampled cone toward the GA.

Our combined sample of spirals, S0s, ellipticals, and clusters contains a total of 973 galaxies in 493 objects. This sample was used in DBF as the "mask" through which the N-body simulation was "observed" and analyzed. In BD90 and DB90, we used an earlier data set consisting of 526 objects containing 896 galaxies in which the DF sample was only partly represented and not yet grouped with 7S, and the A89 field galaxies and the LC galaxies were not included.

Figure 1 shows the distribution of objects at their measured positions with their observed radial peculiar velocities. The large-scale view in Figure 1*a* shows the whole sample out to $\pm$6000 km s^{-1} distance in each direction (more distant objects are used but not shown); Figure 1*b* shows a smaller scale view of just the nearby spirals. Each page consists of nine panels corresponding to nine planar cuts through a sphere. The three panels in the central column are the orthogonal planes passing through the origin in Supergalactic coordinates, where $Z = 0$ (Lsc) is the plane of the Local Supercluster (also called LSC) and $Y = 0$ (Gal) is very nearly the Galactic plane. The columns

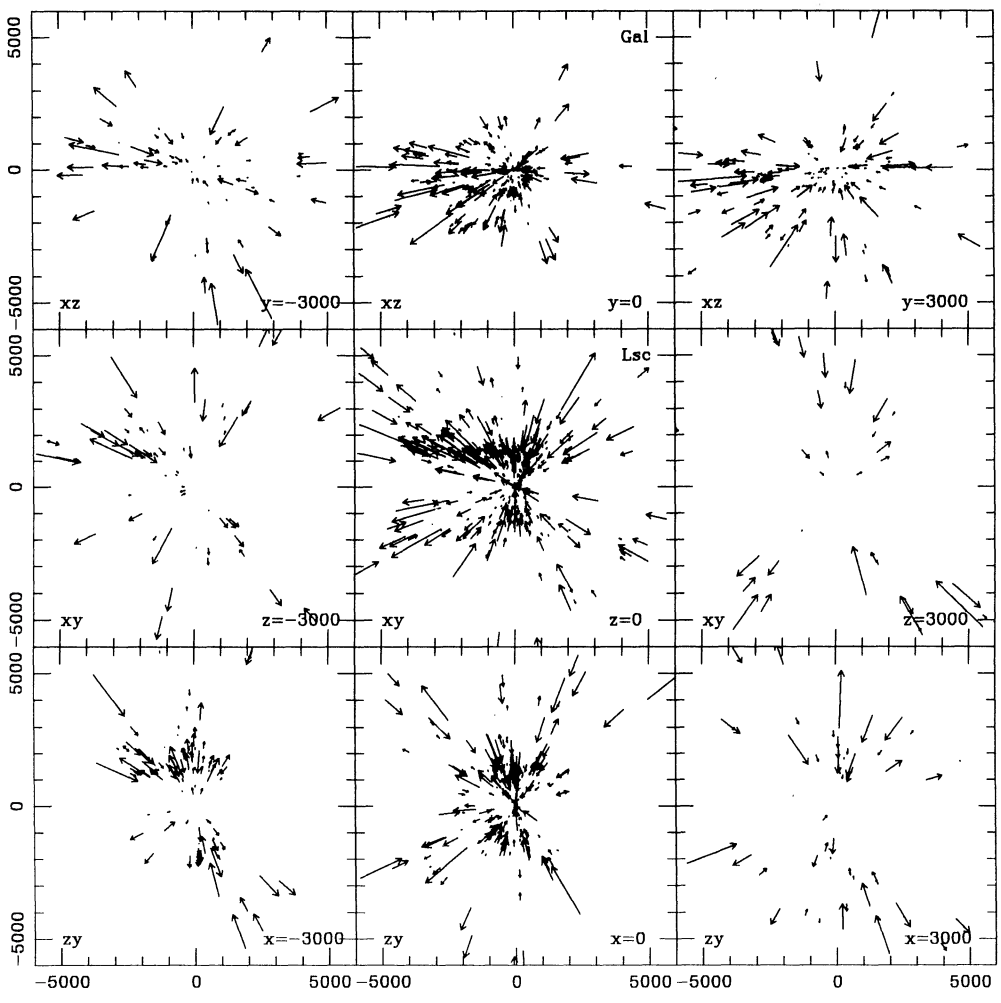

FIG. 1*a*

FIG. 1.—The observed radial peculiar velocities of objects in nine slices. X, Y, Z are Supergalactic coordinates, with the Milky Way at $X = Y = Z = 0$. The vectors are placed at the measured distances of the objects and show the velocity components projected onto the indicated planes. Distances and velocities are both in km s^{-1}. The three horizontal rows each give parallel offset views in thick but non-overlapping slices centered at the indicated positions. The Local Supercluster plane (Lsc) is $Z = 0$ and the Galactic plane (Gal) is nearly $Y = 0$. (*a*) All of the data within $\pm$6000 km s^{-1} in the indicated directions, including field spirals, spiral clusters, field E/S0s, and E/S0 clusters. Each slice shows the data within $\pm$1500 km s^{-1} of the designated plane. (*b*) Spirals and nearby spiral clusters only. The spacing and thickness of the slices is one-half that of (*a*).

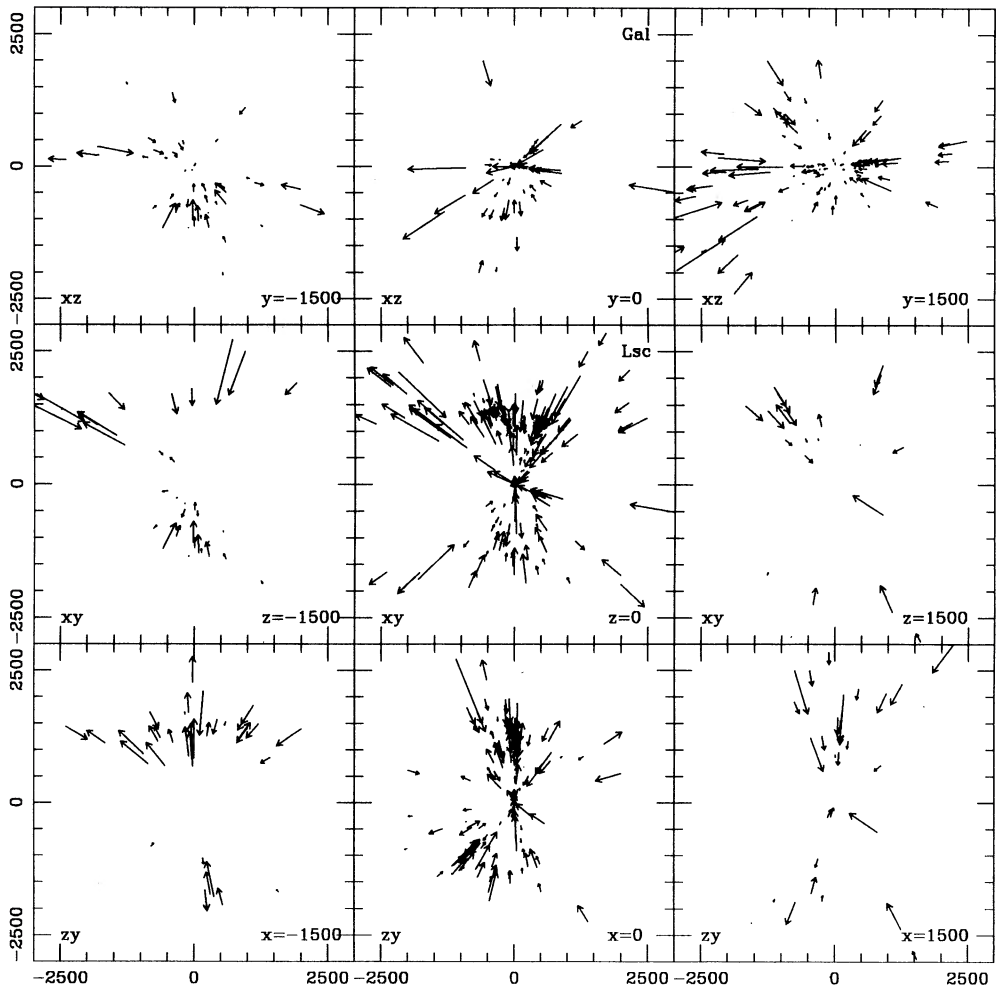

FIG. 1*b*

to the left and right of center give slices parallel to these central planes, displaced by ± 3000 km s^{-1} in Figure 1*a* and ± 1500 km s^{-1} in Figure 1*b*, with thicknesses of 3000 km s^{-1} and 1500 km s^{-1} respectively. The radial velocity components projected onto each slice are shown by the arrows in each plot.

Perhaps the most interesting panel is the LSC plane (center). Note how sparse the spatial distribution is even in this high-density slice. The Galactic zone of obscuration is apparent as the empty angle about $Y = 0$. The GA region, toward Hydra-Centaurus ($X < 0$, $Y > 0$, $Z \approx 0$), is heavily populated, partly because there are several clusters there but mostly because of the samples of DF and LC, which were selected in that region. The number density (i.e., completeness) drops steeply with radius in all directions. In the heavily populated regions in the vicinity of Virgo ($X = -300$, $Y = 1300$, $Z = -50$) and Hydra-Centaurus, the mean separation between neighbors is less than 300 km s^{-1}, while within the sphere of radius 6000 km s^{-1} there are many empty regions where the separation between neighbors exceeds 2000 km s^{-1}.

III. SMOOTHING

The first step of the POTENT analysis is interpolating the observed radial velocities u_i at the object positions $\mathbf{r}_i$ into a smoothed radial velocity field, $u(\mathbf{r})$, using a tensor window function (DBF, § IV). The smoothing averages over regions where vorticity might be present and reduces nonlinearity by averaging over the small-scale structure, but its main purpose is to reduce the large peculiar velocity errors of individual objects by averaging nearby points. The goal of the smoothing procedure is to obtain an optimal velocity field with minimum bias due to nonuniform spatial sampling and minimum variance arising from measurement errors and the sparseness of the galaxy distribution.

Our estimate for the radial velocity u at position $\mathbf{r}$, smoothed with a window function W, is

$$u(\mathbf{r}) = \sum_i \tilde{W}(\mathbf{r}, \mathbf{r}_i) u_i \,, \tag{3a}$$

$$\tilde{W}(\mathbf{r}, \mathbf{r}_i) \equiv [\hat{\mathbf{r}} \cdot \mathbf{A}^{-1}(\mathbf{r}) \cdot \hat{\mathbf{r}}_i] W(\mathbf{r}, \mathbf{r}_i) \,,$$

$$\mathbf{A} \equiv \sum_i W(\mathbf{r}, \mathbf{r}_i) \hat{\mathbf{r}}_i \hat{\mathbf{r}}_i \,. \tag{3b}$$

In effect, we are computing the maximum likelihood "bulk flow" solution within a window defined by W in the vicinity of $\mathbf{r}$. Tensor smoothing is required because we are averaging radial velocities from different directions $\hat{\mathbf{r}}_i$ (Regös and Szalay 1989). In equation (3a) the tensor projection is absorbed into the normalized scalar $\tilde{W}$. It is worth mentioning that a tensor smoothing similar to equation (3) can also provide formally, an estimate for the tangential components of the velocity field. However, when the window size is smaller than r, this estimate

carries a larger error than the estimate of the radial component, so it is useful only close to the origin. Therefore, only the smoothed *radial* velocity of equation (3) is used as input for the potential flow analysis below.

Based on our error analysis and after some trial-and-error effort, we have adopted the following two window functions (DBF, § IV):

$$W_F(\mathbf{r}, \mathbf{r}_i) = \frac{R_4^3(\mathbf{r}_i)}{\sigma_i^2} \exp\left[-\frac{|\mathbf{r}-\mathbf{r}_i|^2}{2R_w^2}\right], \quad (4a)$$

$$W_V(\mathbf{r}, \mathbf{r}_i) = \frac{R_4^3(\mathbf{r}_i)}{\sigma_i^2} \exp\left[-\frac{|\mathbf{r}-\mathbf{r}_i|^2}{2R_5^2}\right]. \quad (4b)$$

$R_4(\mathbf{r}_i)$ is the distance from object i to its fourth nearest neighbor. The factor $R_4^3(\mathbf{r}_i)$ weights the contribution from u_i by the inverse of the local density of objects in the vicinity of $\mathbf{r}_i$. This weighting serves to correct, approximately, the *sampling gradient bias* in $u(\mathbf{r})$ (relative to a uniform volume average) that is caused by gradients in the effective sample selection function, whereby the information in well-sampled regions propagates into sparsely sampled regions. The volume out to the fourth nearest neighbor was chosen as a correction factor after experimentation with an N-body simulation. The additional weighting by σ_i^{-2} minimizes the *measurement variance* in u due to distance errors.

In this paper, we take σ_i to be a given fraction of the estimated distance as measured by the redshift-independent distance estimator ($\Delta = 0.21$ and 0.16 for E/S0s and spirals, respectively). This choice of distance (as opposed to observed radial velocity) is important in eliminating homogeneous Malmquist bias, as explained in DBF. To this base error, mentioned already in § II, we add in quadrature a constant "field" dispersion, $\sigma_f = 150$ km s^{-1}, the value estimated for spiral galaxies by Faber and Burstein (1988). The addition of σ_f allows us to use nearby galaxies in the sample, including M31 and M32, without giving them excessive weight. (In BD90 and DB90 we took σ_i to be a constant fraction of the total redshift velocity of the galaxy in the Local Group frame, with no additional σ_f.)

The radius of the Gaussian, R_w, defines the spatial extent of the smoothing window. The first window, W_F, has a fixed effective smoothing radius. In practice, this must be small enough to control the sampling gradient bias but large enough to reduce the measurement variance to an acceptable level, requiring a difficult balancing act. The second window, W_V, has a spatially varying smoothing radius defined by the distance from $\mathbf{r}$ to the fifth nearest neighboring object, R_5. This window controls the variance by including a fixed number (~ 5) of objects in the sum, at the expense of large sampling gradient bias in poorly sampled regions. All window functions necessarily have advantages and disadvantages. The variable window gives us better resolution in the well-sampled regions while not asking too much where the data are sparse. However, this window depends strongly on the sample used and so is inconvenient for comparison with results from other samples or theoretical predictions. The fixed window requires compromises, but it is a good choice for quantitative comparison with other data and with theory, as it approximates uniform Gaussian smoothing. The pros and cons of various window functions are discussed in detail by DBF.

Figure 2 shows the weights assigned to the objects whose radial peculiar velocities were shown in Figure 1. The area of each symbol is proportional to R_4^3/σ_i. The effect of volume-weighting is obvious: points in dense regions are smaller, on average, than those in sparse regions. The largest spiral cluster point in the $Z = -3000$ slice is Abell 400; the other strongly weighted spiral cluster in this slice is Cancer, which also appears in the $X = 3000$ and $Y = 3000$ slices. The large black square in the $Y = 0$ and $Z = 0$ slices is the Perseus cluster. The slightly smaller black square in the $Z = -3000$ and $Y = 3000$ slices is Abell 569; although it contains many fewer measured ellipticals than Perseus (5 vs 18), its even greater isolation gives it comparable weight. The volume weighting is necessary to minimize the sampling gradient bias, but one must beware that the predominance of one object can lead to artificially coherent flows in sparsely sampled regions.

Figure 3 shows three versions of the smoothed radial velocity field $u(\mathbf{r})$. Figure 3*a* is the result of smoothing with W_V, where $R_w = R_5$ unless $R_5 < 300$ km s^{-1} or $R_5 > 2000$ km s^{-1}, in which case we set $R_w = 300$ or 2000 km s^{-1}, respectively. (In practice, we always limit the variable window function this way to avoid undersmoothing or excessive bias.) Figure 3*b* uses W_F with a large smoothing radius, $R_w = 1200$ km s^{-1}. Figure 3*c* shows the result on a smaller scale for smoothing with W_F and a small smoothing radius, $R_w = 500$ km s^{-1}. These figures may be compared with Figure 1 to see how our smoothing makes use of the individual objects. Note the clear infall pattern around the GA region in the upper left quadrant of the Supergalactic plane of Figures 3*a* and 3*b*. Note also the infall pattern in Figure 3*c* into Virgo ($X \approx 0$, $Y \approx 1300$, $Z \approx 0$), seen in the LSC and $X = 0$ planes, especially along the Y-axis. Nearly all of the errors of the final three-dimensional velocity field are already present at this stage of the analysis and are evident especially as the large, clearly spurious arrows in the sparsely populated, outer regions of the fixed-window field.

IV. RECOVERED POTENTIAL, VELOCITY, AND DENSITY FIELDS

We now apply our potential flow algorithm to the smoothed radial velocity field of the combined data set to reconstruct the full three-dimensional fields. We follow the same procedures with the data as were used by DBF (§ V) with an N-body simulation. Our results and error maps are presented in this section and are discussed in § V.

To calculate the velocity potential and velocity field we use the Eulerian technique based on equations (1) and (2) and described in detail by DBF (§ III*a*). Note that the velocity potential calculated this way at a given radius from us depends only on the smoothed radial velocity data interior to that radius, unlike the gravitational potential, which depends on the mass density everywhere. With the variable window function, W_V ($R_w = R_5$ between 300 and 2000 km s^{-1}), we use a grid in spherical coordinates of 16 equal radial shells out to a radius of 7000 km s^{-1}, 24 latitude circles and 24 longitude circles. With the fixed window W_F, we set $R_w = 1200$ km s^{-1} and use 10 radial shells and 16 latitude and longitude circles. These grids are fine enough to resolve all of the features retained by the smoothing windows. The final fields are evaluated on a cubic grid of spacing 500 km s^{-1} using cloud-in-cell interpolation from the spherical grid.

Figure 4 shows the velocity potential contours in the nine planes with the same geometry as Figures 1–3. The potential is set to zero at the Milky Way ($X = Y = Z = 0$). Note the dominance of one huge potential well—the Great Attractor (centered at $X \approx -4500$, $Y \approx 2000$, $Z \approx 500$). On smaller scales the potential maps are relatively featureless, as expected.

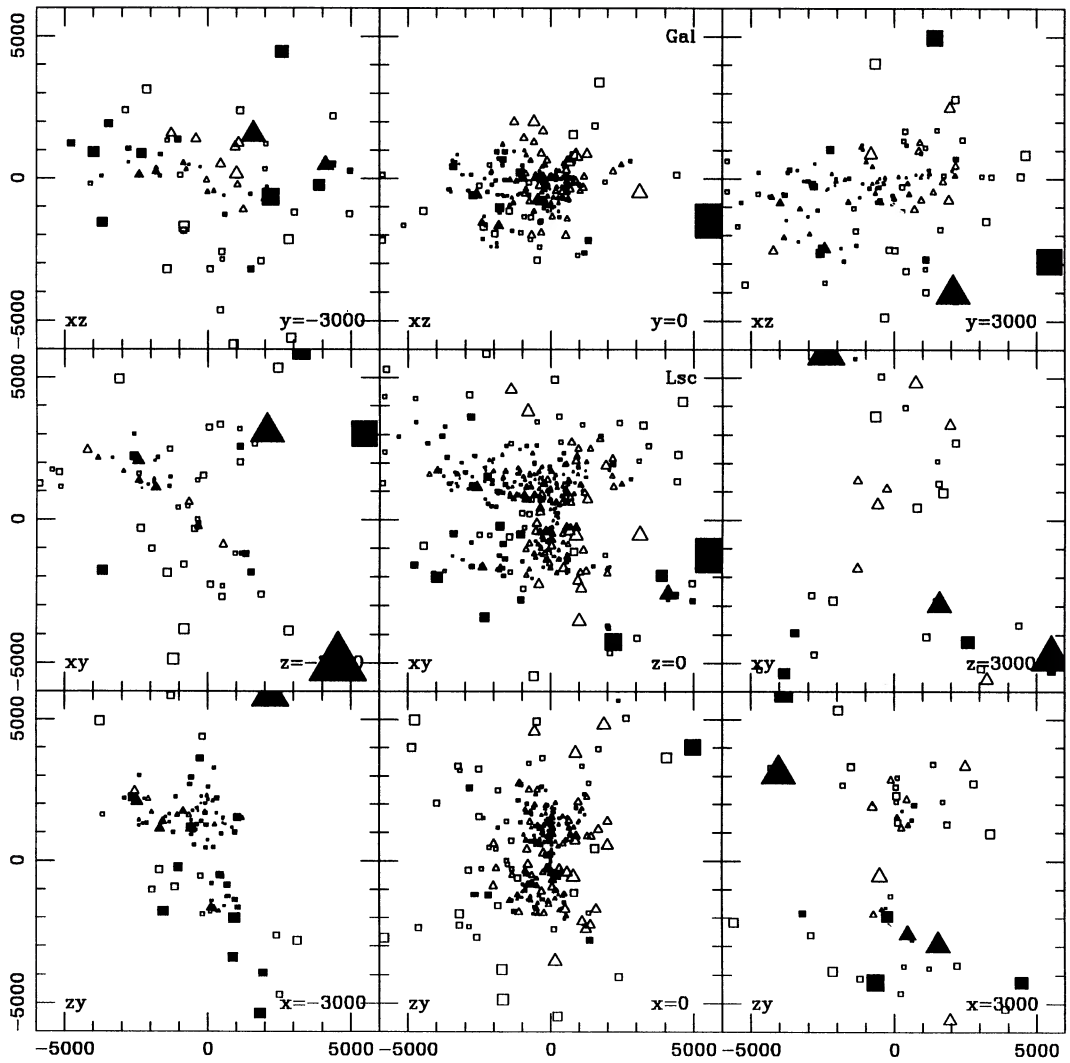

FIG. 2.—Weights for the objects appearing in Fig. 1*a*. Open symbols are individual galaxies and filled symbols are groups. Triangles are spirals with IRTF distances while squares are ellipticals and S0s with $D_n - \sigma$ distances. The area of each symbol is proportional to the weight assigned to the object's measured peculiar velocity in the smoothed radial velocity field. Several objects with large weight are identified in the text.

The differences between the results with the two different windows are not very pronounced.

To assess the errors in the reconstructed potential, we perform Monte Carlo simulations as described by DBF (§§ IV*d* and V). The largest source of error is simply the random distance error of each data point. We construct 100 artificial redshift-distance samples in which the distance (and hence peculiar velocity) of each object is scattered using an independent zero-mean Gaussian random number of standard deviation equaling the estimated standard deviation of each measurement. We also scatter each redshift with a Gaussian of standard deviation $\sigma_f = 150$ km s^{-1} in order to mimic the effects of small-scale sampling fluctuations. For each artificial sample we reconstruct the potential and velocity fields and then construct maps of the mean and standard deviation of these fields. The standard deviation provides our error estimates, while the mean of the noise simulations is useful for diagnosing Malmquist bias (DBF).

Figure 5 shows contours of the standard deviation of the velocity potential using the fixed window W_F. The contour spacing is the same in Figures 4 and 5, so one can see that over most of the volume the signal-to-noise ratio is fairly large. Note that the error contours are flattened toward the Supergalactic plane $Z = 0$ because there are fewer galaxies outside of this plane. The error map in the LSC plane compares very well with the map of DBF (Fig. 11) based on the N-body simulation. This is not surprising, in spite of the fact that the velocity field of the simulation is different from that of the real data, because the same sampling positions and distance errors were used in the two cases. We conclude that our noise simulations, based either on the data or on a simulated velocity field, provide a reliable estimate of the effects of random distance errors on the reconstructed fields.

Figure 6 shows the reconstructed three-dimensional velocity field projected onto the nine planes. The radial velocity components exactly equal the radial velocity fields of Figure 3. Compared with the potential, the velocity field reveals more features on small scales, and the difference between the variable and fixed windows becomes more noticeable. Note, for example, the difference in the collapse pattern in the central regions of the GA. With W_V (Fig. 6*a*), the smoothing radius drops down to 300 km s^{-1}, revealing peak velocities ≈ 1000

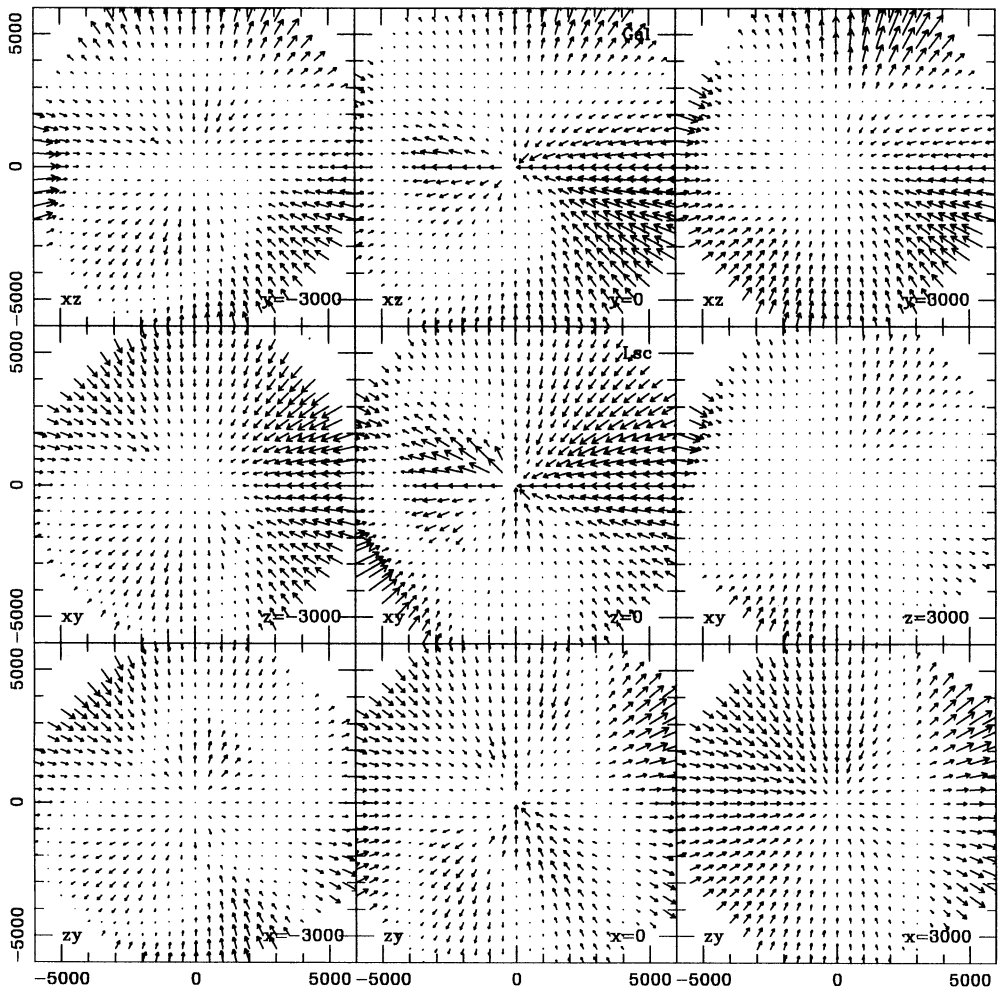

FIG. 3a

FIG. 3.—The smoothed radial velocity field constructed using a tensor window function, at the points of a cubic grid in the nine planes corresponding to the slices of Fig. 1, projected onto the planes. (*a*) Smoothing by the variable window W_V, with smoothing radius equaling the distance to the fifth nearest object except being constrained to lie in the range 300 to 2000 km s^{-1}. Only the points within a sphere of radius 7000 km s^{-1} used in the analysis are shown. (*b*) Smoothing by the fixed window W_F with Gaussian smoothing radius R_w = 1200 km s^{-1}, also inside 7000 km s^{-1}. (*c*) Smoothing by the high-resolution fixed window with R_w = 500 km s^{-1}, inside a sphere of radius 3000 km s^{-1}. All the data are used in each case but spirals dominate the region within 3000 km s^{-1}.

km s^{-1} and a dramatic caustic between the LG and the GA center. With W_F (Fig. 6*b*), the smoothing radius is fixed at 1200 km s^{-1} so that the collapse pattern is heavily smoothed, with peak infall velocities of only $\approx$600 km s^{-1}. The opposite effect is apparent in several poorly sampled regions, such as those at large Z. With W_V, the smoothing length is stretched enough always to allow a few objects in the window, resulting in a reasonably smooth and quiet velocity field where the data are sparse. In such regions the fixed window is clearly too small, resulting in large, chaotic features that often depend on just a single noisy data point. Figure 6*c* repeats the velocity field with W_F in which regions of large uncertainty (see below) have been excluded. These are the only regions to which we attach physical significance based on the current data.

To illustrate the effect of noise (distance errors) in the data, we show in Figure 7 the velocity field reconstructed from one Monte Carlo noise simulation using the fixed window. The noise features are much more pronounced than they are in the original data (Fig. 6*b*), and some new spurious features are added (e.g., $X \approx -5000$ in the $Z = 3000$ slice). If the original velocity field were pure noise and we add uncorrelated noise of the same amplitude, then the vectors would increase in length by a factor of 1.4 (rms), and the direction would be shifted by an average of only 45°. This is roughly what happens at large distances where the errors dominate the underlying true velocity field. Over much of the volume, however, the signal evidently dominates the noise.

Figure 8 shows contours of the standard deviation of velocity for the fixed window using the same 100 Monte Carlo simulations as Figure 5. The error map in the LSC plane again agrees well with that obtained from the N-body simulation by DBF. In the well-sampled regions (out to 3000 km s^{-1} in most directions and nearly 6000 km s^{-1} toward the GA), the rms error is less than 300 km s^{-1}, but the errors exceed 1000 km s^{-1} in some poorly sampled regions. The errors are smaller and more uniform with the variable window function (not shown).

Besides suffering from large random errors (measurement variance), our reconstructed fields are also subject to *biases*. In particular, the sampling gradient bias and Malmquist bias

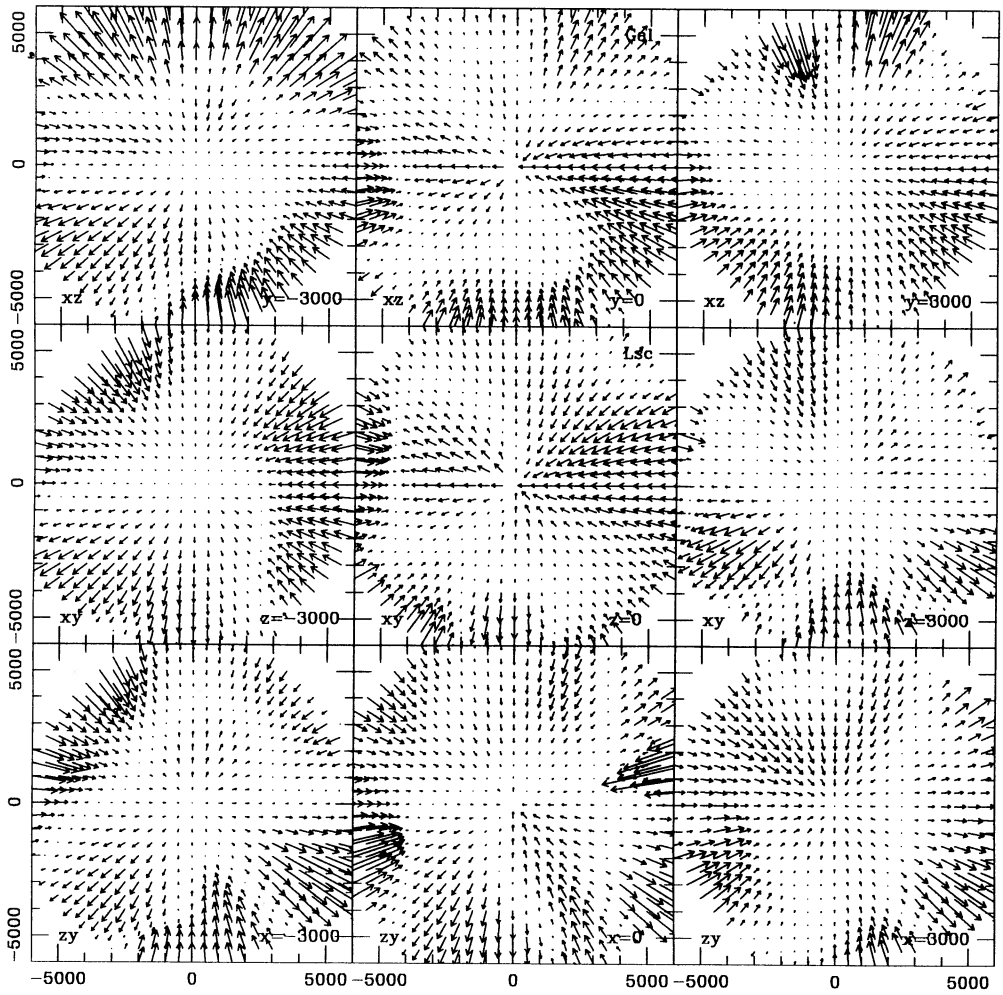

FIG. 3*b*

cause concern (DBF). From the data themselves we cannot separate the bias and variance errors. However, in DBF we showed that the residual Malmquist bias can be estimated from Monte Carlo simulations and can even be removed if the sample selection function is accurately known. Because the effective selection function of our combined, heterogeneous sample is unknown, we cannot remove this bias here. Nevertheless, we trust the conclusion of DBF, based on Monte Carlo simulations, that the residual Malmquist bias errors in the velocity field are less than 200 km s^{-1} nearly everywhere for the $R_w = 1200$ km s^{-1} fixed window. This error is small enough to be of little concern except as noted below in § V.

The sampling gradient bias is more difficult. Since it arises from a coupling of gradients in the true velocity field and the selection function, neither of which is known, it is difficult to assess from the data. However, in DBF we showed that sampling gradient bias can be identified and minimized using Monte Carlo simulations based on the known velocity field of an N-body simulation. We showed that with our volume weighting scheme (weight $\propto R_4^3$), the bias was generally much smaller than the uncertainty due to distance errors. There are, however, a few very empty regions where sampling bias might be severe enough to generate coherent artificial flows having no physical reality. These include regions at low Galactic latitude and voids in the galaxy distribution away from the Supergalactic plane. Being unable to quantify the sampling gradient biases in these regions at this stage, we can simply exclude very empty regions from further analysis, based on some criterion for "emptiness." For example, we can exclude all points where the distance to the nth nearest neighboring object is greater than some value. In Figure 6*c* above, we applied such a mask, excluding all regions that are either too noisy or too empty. The exclusion criteria in this case were that the standard deviation of the velocity exceed 400 km s^{-1} or that R_1, the nearest neighbor distance, exceed 1200 km s^{-1}. These criteria appear to satisfactorily remove all the noisy regions referred to earlier.

Obtaining the *density* field requires more effort. In the linear approximation, the fluctuations in mass density can be obtained from the velocity field using the linearized continuity equation, $\delta \approx -\nabla \cdot \boldsymbol{v}/(H\Omega^{4/7})$ (e.g., Peebles 1980; Lightman and Schechter 1990). However, in order to recover structure on scales of order 1000 km s^{-1} and smaller, where $\langle \delta^2 \rangle$ might be of order unity or larger, we would prefer to use an approximation that is more accurate for moderately nonlinear evolution. In particular, we should not ignore displacements of matter in the comoving frame, as the linear approximation does. Equivalently, we must take into account the fact that the gravitational potential is not simply proportional to the velocity potential.

To solve this problem, we reconstruct the density field using

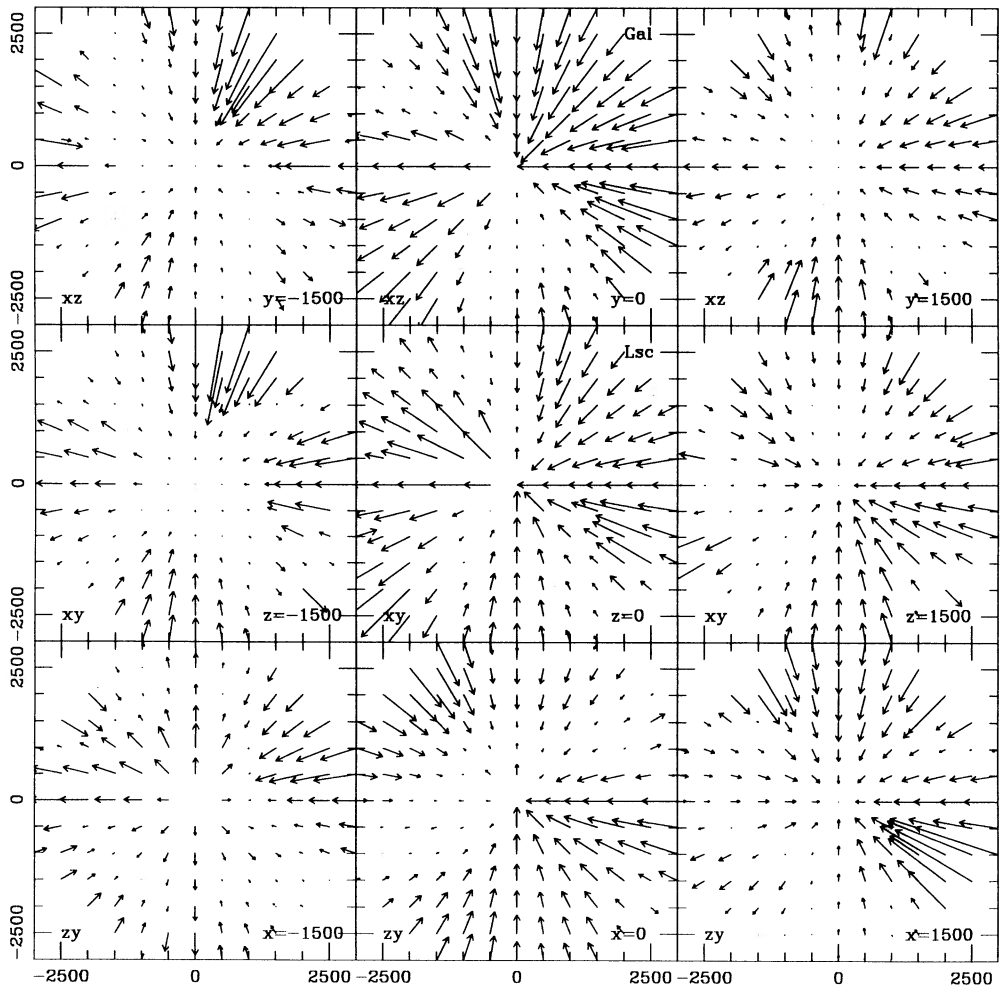

FIG. 3*c*

the iterative Lagrangian procedure based on the Zel'dovich (1970) approximation as described in BD and DBF (§ II*b*). This technique makes use of the one-to-one correspondence between the initial (i.e., Lagrangian) and final (i.e., Eulerian) positions of particles. The procedure solves iteratively for the linear displacement field required to yield the observed smoothed radial velocity field $u(r)$, subject to the constraint that the Lagrangian displacement field be irrotational. As discussed in DBF, the conditions that the Lagrangian displacement field and the Eulerian velocity field be irrotational are equivalent in the absence of orbit-crossing. The Lagrangian procedure is preferable for determining the density since we can use the displacement field to compute the density by displacing equal-mass particles from a uniform cubic grid. The final density for the contour plots is computed by counting particles in a spherical window of Gaussian radius 500 km s^{-1} about each grid point, the grid points being spaced by 250 km s^{-1}. Because of this extra smoothing, the effective smoothing radius for our density reconstructions is larger than that for the potential and velocity. We estimate the effective Gaussian smoothing radius for our fixed window to be between 1300 and 1500 km s^{-1}. To reconstruct the density from the velocity, it is necessary to assume a value for Ω. For the present we arbitrarily assume $\Omega = 1$ and note that, if $\Omega < 1$, we have underestimated the amplitude of the density perturbations. If the displacements are small enough for the linear approximation to be adequate, the estimated density contrast scales with Ω approximately as $\Omega^{4/7}$. We will investigate the effect of assuming $\Omega \neq 1$ in subsequent work.

Figure 9 shows the reconstructed mass density field using the two different window functions. The spherical grids used to represent the potential (now in Lagrangian space) have the same numbers of grid points as for the Eulerian potential and velocity reconstructions given above. We have not plotted the density beyond a radius of 6000 km s^{-1} because displacements at the outer edges can carry the particles more than 1000 km s^{-1} from our outer Lagrangian radius of 7000 km s^{-1}. The density contour maps reveal still more small-scale structure than do the velocity maps, and the differences between the two windows are even more pronounced. The main features, such as the GA density peak at $X \approx -4500$, $Y \approx 2500$, $Z \approx 500$, can be anticipated from the velocity field maps (Fig. 6), although one should note that the three-dimensional divergence is needed for the density while only two components of velocity are shown in each panel. It is also interesting to note that density peaks need not correspond to potential minima, and vice versa. Superposing a uniform velocity field does not change the density but it adds a constant potential gradient

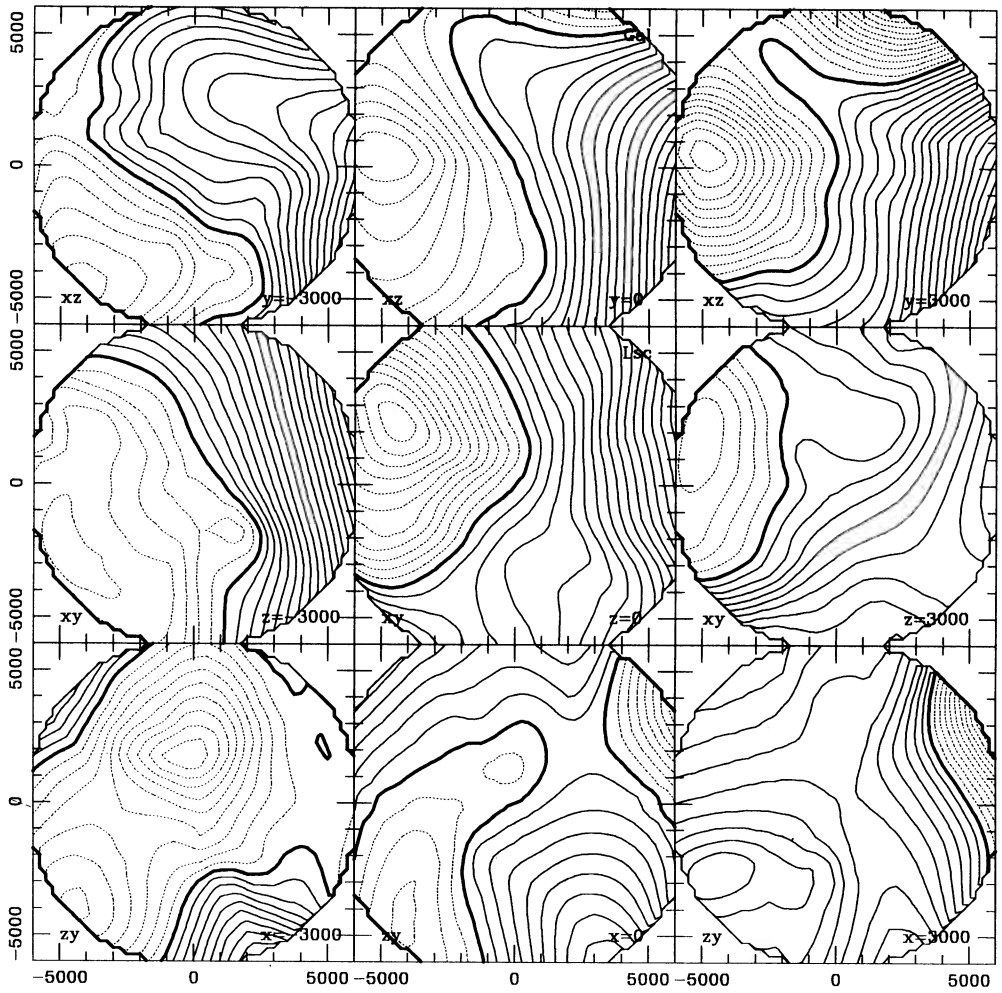

FIG. 4*a*

FIG. 4.—Reconstructed velocity potential field in the nine planes of Fig. 3. Contour spacing is 2.5×10^5 (km s^{-1})^2, with positive contours solid and negative contours dotted. The potential is set to zero (heavy contour) at the origin. (*a*) Smoothing with W_V as in Fig. 3*a*. (*b*) Smoothing with W_F as in Fig. 3*b*.

that can hide the effect on the potential of a density peak. We find it misleading to look at just the density or the potential field; both are useful for interpreting the cosmography.

Figure 10 shows the density from one Monte Carlo noise simulation with W_F. From comparison with Figure 9*b*, we see that many features appear to be robust, such as the GA and the low-density region in the $X < 0$, $Y < 0$ quadrant. The random errors in the reconstructed density field are quantified in the standard deviation maps of Figure 11, based on 20 Monte Carlo simulations. Note that the contour spacing in Figure 11 is half that in Figure 10. The errors are similar to those estimated by DBF using the N-body simulation but they are somewhat higher toward the GA and other density peaks. This may be due in part to fluctuations arising from the small number of density noise simulations, which are, the way we do them here, much more time-consuming than the potential and velocity simulations. In many of the well-sampled regions the rms errors in $\delta\rho/\rho$ are less than 0.2 and are significantly smaller than the signal. The density contrast at the peak of the GA, with effective Gaussian smoothing radius ≈ 1400 km s^{-1}, is $\delta\rho/\rho = 1.2 \pm 0.4$ (assuming $\Omega = 1$). The signal-to-noise ratio appears to be better than that of the reconstructed N-body simulation of DBF, mainly because the unbiased cold dark matter simulation had smaller amplitude density perturbations (with a rms of 0.2 for a Gaussian smoothing radius of 1300 km s^{-1}) than the data indicate for the real universe. However, outside of the Supergalactic plane, most of the strong positive-density contrast features beyond 4000 km s^{-1} are suspicious.

Summarizing the main differences among the three recovered fields, we note that the potential field, $\Phi(\boldsymbol{r})$, is rather quiet and robust; it carries relatively small errors but smooths over small-scale features, being affected mostly by the large-scale, linear fluctuations. The velocity field, $\boldsymbol{v}(\boldsymbol{r})$, resolves intermediate-scale features better, but with generally larger uncertainties. The density field, $\rho(\boldsymbol{r})$, is sensitive to still smaller-scale structures and even resolves some nonlinear features. However, its uncertainty is largest of all. These trends are understandable. The potential is obtained by integrating a noisy velocity field, while the density effectively differentiates the velocity field. If the velocity errors are Poisson, the power spectrum of the noise component of the velocity field is $P_v(k) \propto k^0$, while, for a Harrison-Zel'dovich power spectrum, the power spectrum of the signal is $P_v(k) \propto k^{-1}$. If anything, the measured velocity field appears to have even more power than this on larger scales. The signal thus dominates the noise on large scales, where the potential is the most sensitive and

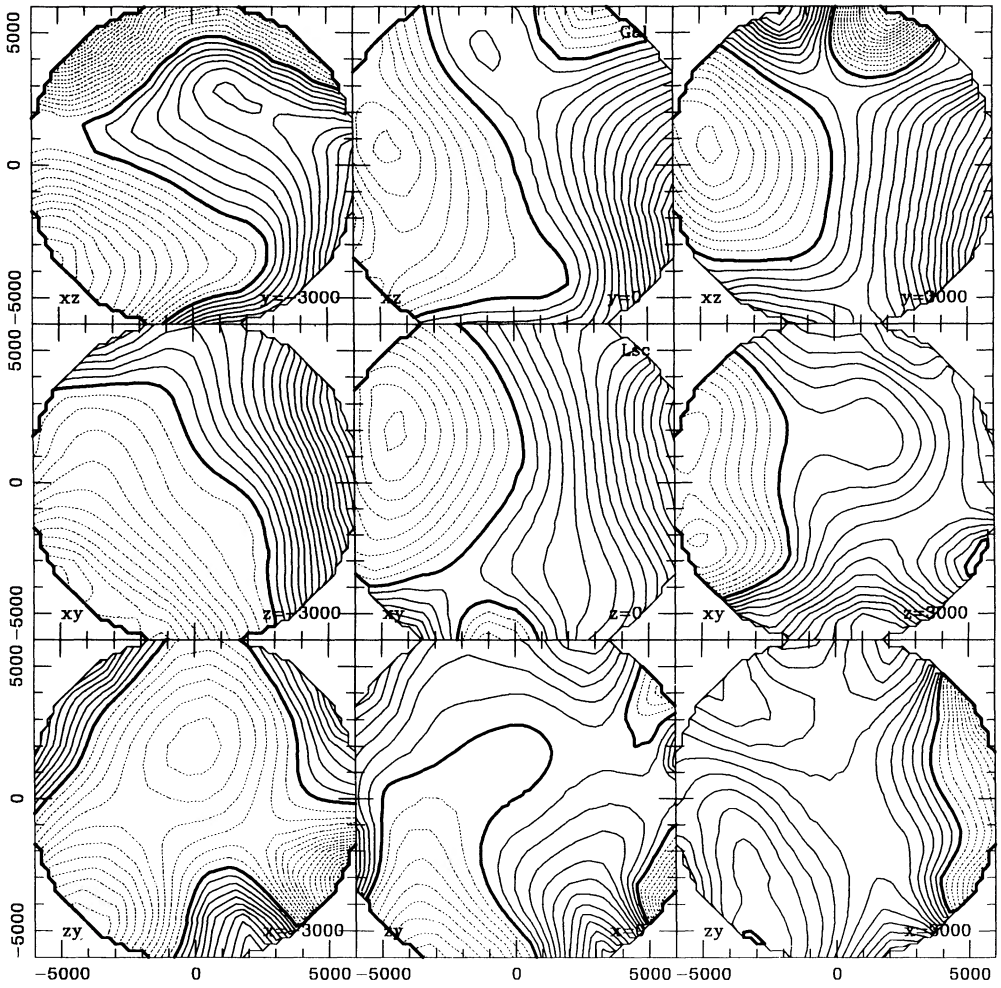

FIG. 4*b*

the density is the least sensitive, with power spectra related by $P_\rho(k) \propto k^2 P_v(k) \propto k^4 P_\phi(k)$.

Based on the error analysis presented here and in DBF, we conclude that, in the absence of unknown large systematic errors, the fields recovered by POTENT have a sufficiently large signal-to-noise ratio to provide a meaningful three-dimensional picture of large-scale structure. The uncertainties in the recovered density field, in particular, are smaller than our initial expectations. The fixed-window maps with $R_w = 1200$ km s^{-1} appear to be reliable enough to use for further statistical analysis, once undersampled regions are excluded. Detailed Monte Carlo simulations will still be needed for appropriate comparison to theoretical predictions and to other data, because we do not know the *a priori* probability distribution of the errors of our recovered fields after the data have been processed through POTENT. We are confident that we understand the statistical errors of POTENT well enough to undertake this next stage of analysis.

V. INTERPRETATION OF THE LARGE-SCALE MAPS

For better visual perspective, we show in Figure 12 perspective plots of the reconstructed density distribution in the Supergalactic plane for the two different windows. This figure contains the same information as the central panels of Figure 9 but is somewhat easier to grasp. The Local Group is at the center. The large peak is the GA. Virgo is the minor local hill along the extension (the Virgo Southern Extension) to the right of the GA. The peak below the GA in the variable window map is the Pavo-Indus-Telescopium complex. A low-density region lies in front of the Virgo Southern Extension. A trace of the Pisces cluster is poorly recovered in the lower right corner of the variable window map. The sharp peak in the foreground of the W_F reconstruction is noise.

What do all of the maps tell us about the local cosmography? The most robust feature, visible in all maps, is the large-scale structure coined the great attractor (GA), confirming the original claims of its discoverers (Lynden-Bell *et al.* 1988) based on radial peculiar velocities alone and with many fewer distance measurements than we now have. In the potential maps the GA shows up as an extended, roughly spherical and relatively featureless potential well which dominates the sampled volume. It is apparent in several panels of Figure 3: $Y = 0$, $Y = 3000$, $Z = 0$, $Z = 3000$, $X = -3000$. It is striking that the GA is not a highly concentrated source of gravity. The velocity potential contours are remarkably uniform, with a velocity toward the GA of roughly 600 km s^{-1} (for $R_w = 1200$ km s^{-1}) across a volume at least 6000 km s^{-1} in diameter (Fig. 6*c*). We have not tried to fit a spherical infall model like that of Lynden-Bell *et al.* or Faber and Burstein (1988) since we strongly believe that the full three-dimensional fields are

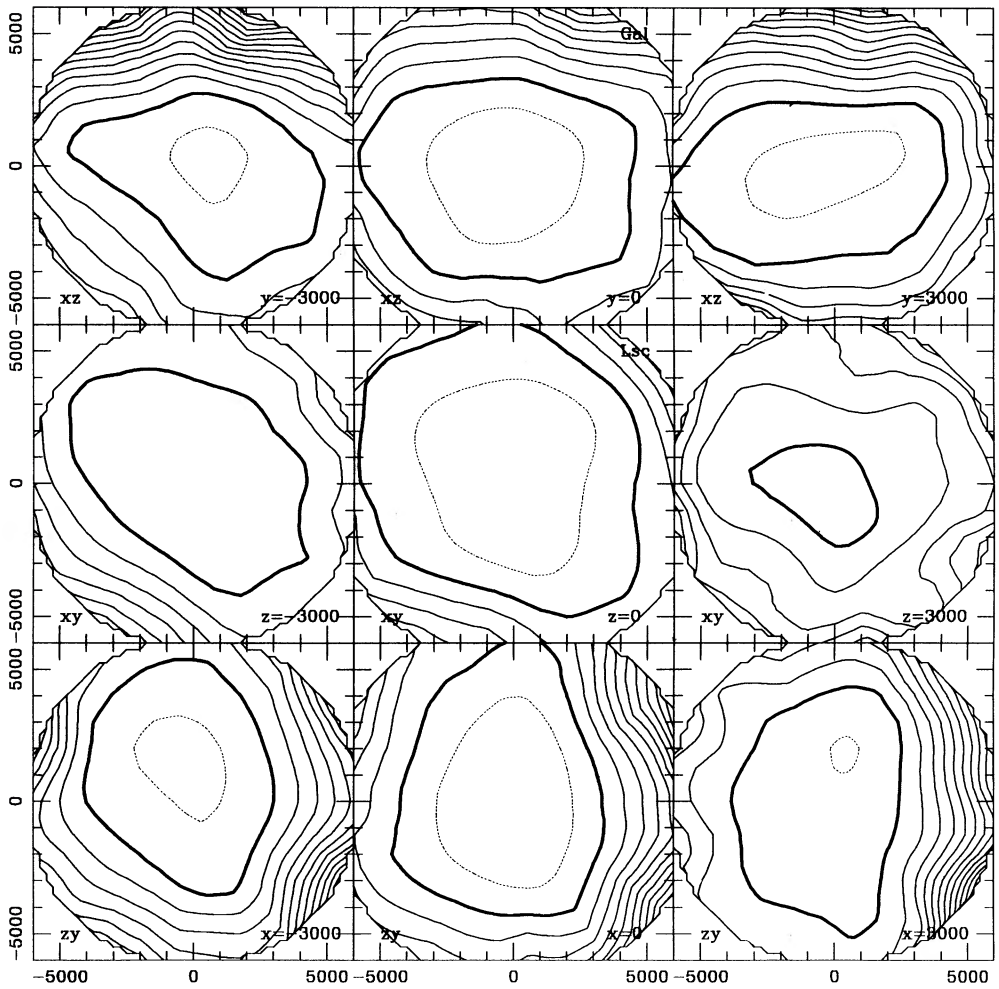

FIG. 5.–Standard error in the potential field with W_F (corresponding to Fig. 4*b*). The standard deviation at each point was obtained from 100 Monte Carlo noise simulations. Contour spacing is the same as in Fig. 4, with the heavy contour at 5.0×10^5 (km s^{-1})^2 and the dotted contour at 2.5×10^5 (km s^{-1})^2.

superior to any such model. Our maps are generally consistent with these models, although one should note that the models were fit without first smoothing the velocity field and our peak velocities are reduced by the smoothing. The velocity and density fields reveal features in and around the GA on smaller scales, as well as other features outside the GA, but the GA density excess extends over perhaps one quarter of the volume within 6000 km s^{-1} distance from the Local Group (Fig. 9*b*). With an effective Gaussian smoothing radius of ≈ 1400 km s^{-1} (Fig. 9*b*), the central region of the GA is a $\delta\rho/\rho = (1.2 \pm 0.4)\Omega^{-4/7}$ peak, centered at $X \approx -4500$, $Y \approx 2500$, $Z \approx 500$. The smoothed density contrast at the LG is (for $\Omega = 1$) $\delta\rho/\rho = 0.1 \pm 0.1$.

The existence of the large-scale GA flow is not affected by the controversial data in the complex Centaurus region itself (Lucey and Carter 1988; Dressler 1988). We have verified that there is very little change when the two Centaurus clusters (Cen 30 and Cen 45) are removed from the data altogether. The peak density excess of the GA in that case is $\delta\rho/\rho \approx 1.1$ (1400 km s^{-1} Gaussian smoothing and $\Omega = 1$), and the center is shifted slightly to $X \approx -4500$, $Y \approx 3000$, $Z \approx 1000$. By studying and comparing Figures 1, 3, and 6, one may see that the GA pattern is evident in the peculiar motions of many groups and galaxies of all Hubble types, extending over a large solid angle and a large range of distances.

The varying window (Fig. 12*a*) allows a higher resolution view of the central regions of the GA. Two infall centers are suggested: a high peak near Centaurus and a somewhat lower peak near the Pavo-Indus-Telescopium (PIT) cluster complex on the opposite side of the Galactic plane, at $Y \approx -2000$. However, the saddle between the GA and PIT peaks could be an artifact of poor sampling in the zone-of-avoidance. As DBF discussed, the density reconstruction can be affected systematically by the sampling gradient bias: $\delta\rho/\rho$ is obtained effectively from the divergence of the velocity field; the velocity field is artificially smoothed in poorly sampled regions like the zone-of-avoidance so that the amplitude of $\delta\rho/\rho$ is underestimated there. It is therefore possible, as suggested by the density recovered with the fixed window, that the superclusters of Hydra-Centaurus and PIT should be regarded as one big super-structure. More peculiar velocities at low Galactic latitudes are needed to answer this question.

With the new Dressler and Faber (1990*a*) data, POTENT reveals a strong apparent signal of infall into the GA from its back side. Recall, however, that, because the density distribution falls off behind the GA, the Malmquist bias discussed in

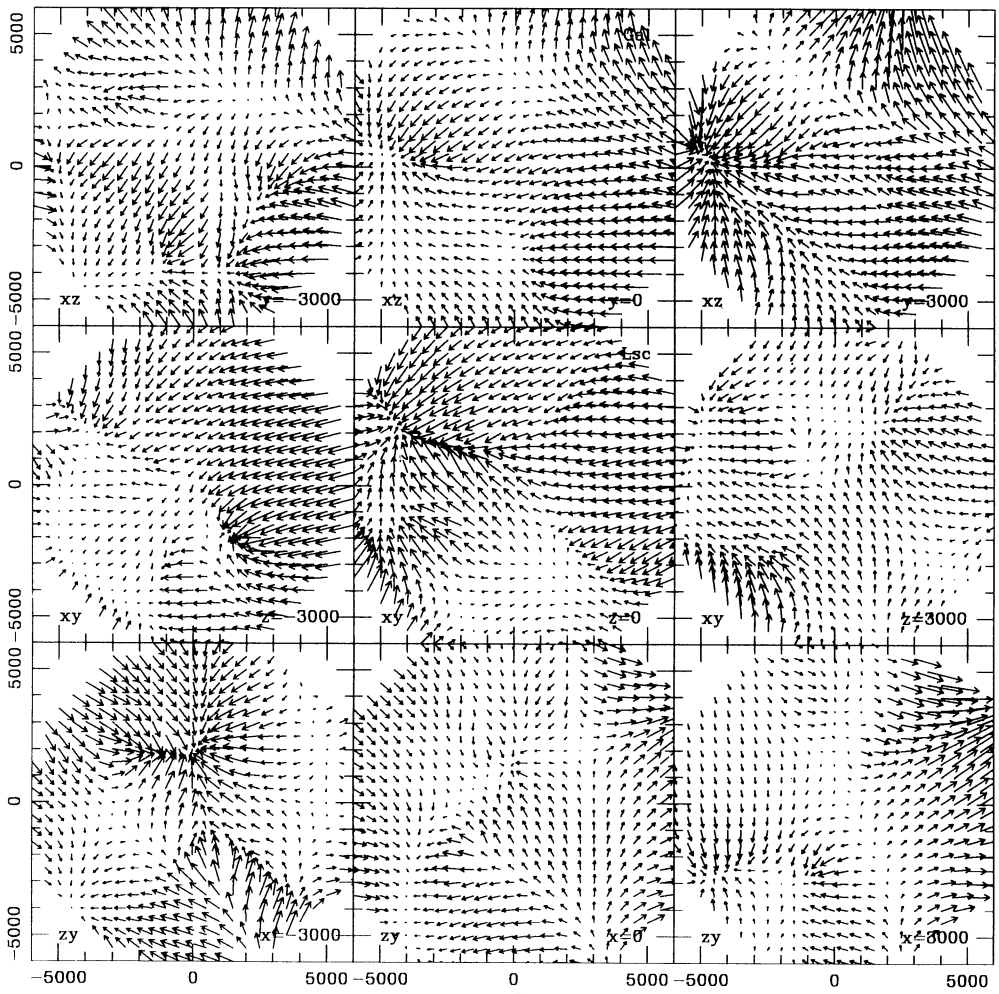

FIG. 6a

FIG. 6.—Reconstructed velocity field evaluated on a cubic grid and projected onto the nine planes. (*a*) W_V. (*b*) W_F. (*c*) W_F, with velocities of large uncertainty excluded. Points are excluded if the standard error from Monte Carlo simulations is greater than 400 km s^{-1} and/or if the region is poorly sampled, with $R_1 > 1200$ km s^{-1}.

DBF might tend to produce a similar, spurious backflow (see also Dressler and Faber 1990*a* and Burstein, Faber, and Dressler 1990). Essentially, if there is a clump of galaxies all at the same true distance and redshift, then distance errors will scatter their measured distances along the line of sight, creating an artificial infall pattern. The amplitude of the infall from the far side of the GA seen here is comparable to the bias and variance errors revealed by Monte Carlo simulations (see Figs. 6*c* and 8 above and Fig. 9 of DBF). Therefore, the reality of this flow needs confirmation based on a deeper data set. A sample of spiral galaxies in that region (Dressler and Faber 1990*b*) promises to provide the required depth.

We determine the direction to the center of the GA infall, defined by the minimum of the velocity potential (i.e., zero peculiar velocity) to be $(L, B) = (156, 9)$ for $R_w = 1200$ km s^{-1}, with an uncertainty of several degrees. For the smaller smoothing length given by the varying window, the direction is (151, 6). For comparison, Lynden-Bell *et al.* determined the GA direction to be (170, −9) based on the bulk motion direction of the entire sample, and Faber and Burstein (1988) obtained (161, −6) from optimizing the direction of the infall center. The latter differs by 16° from the direction given by our fixed window, which is slightly larger than the internal uncertainties of each measurement. Although our result is based on significantly more data in the GA direction, we suspect that much of the difference may come from the fact that the flow model fit by Faber and Burstein does not give a perfect description of the actual flow as revealed by POTENT.

The distance to the center of the GA is also somewhat uncertain. As we vary the smoothing scale and/or the σ_i weights in the window function, the distance to the potential minimum varies between 4000 and 5000 km s^{-1}. This is to be compared to 4350 ± 350 in Lynden-Bell *et al.* 1988 and 4200 ± 350 from Faber and Burstein. Figure 13 demonstrates the effect of changing the weights using the fixed window function. The right panel shows the reconstructed velocity field in the Supergalactic plane when σ_i is taken to be a fraction Δ of the distance as estimated by the recession velocity in the Local Group frame (O for the "old" way as in BD90 and DB90, but with the improved sample). In the left panel (N for "new," as in the rest of the present paper), σ_i is taken to be a constant fraction of the redshift-independent, Malmquist-corrected estimated distance r_i. The former choice would give minimum bias if the galaxies are all concentrated in clumps with no peculiar velocities, but

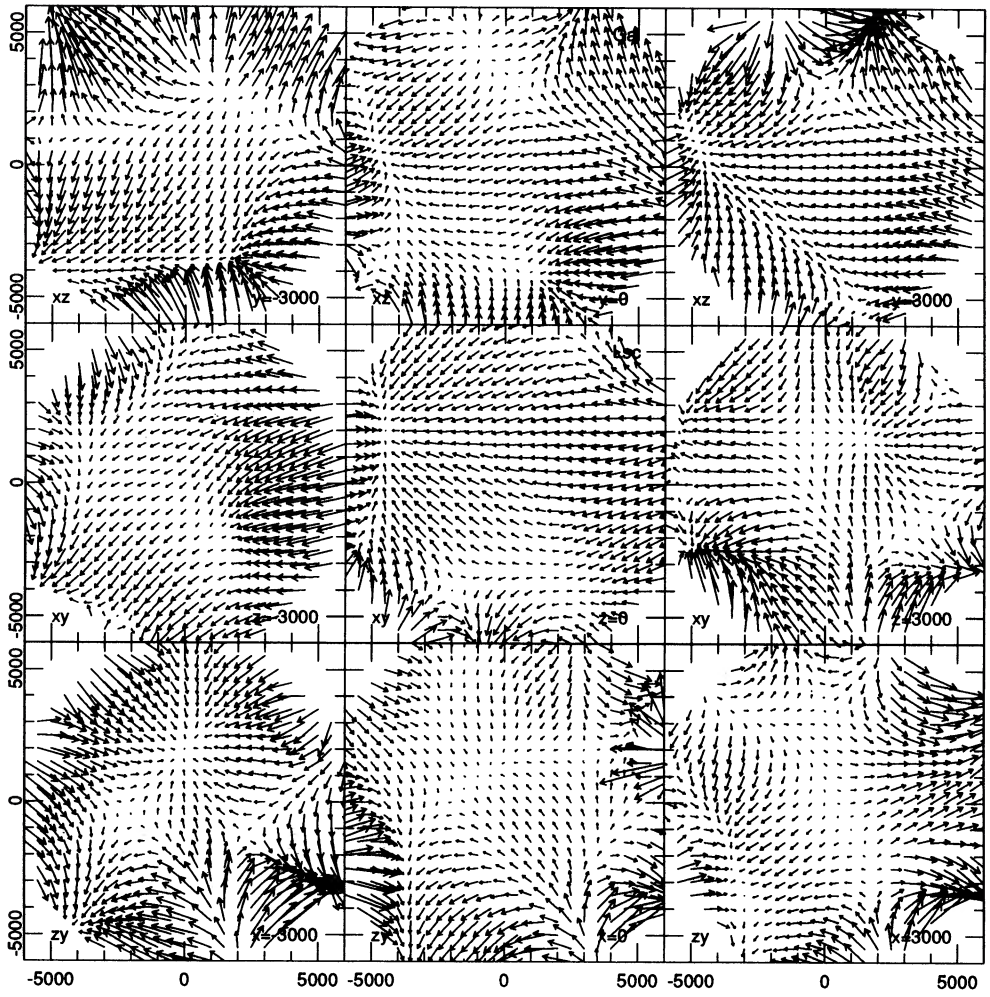

FIG. 6*b*

suffers from a general Malmquist bias in uniform density regions (DBF). The latter choice, by contrast, has no uniform-density bias but suffers from bias in clumpy regions, where it endows clumps of galaxies at the same true distance with artificial positive peculiar velocities. We have chosen to live with this bias, which we can estimate from Monte Carlo simulations, rather than to mix questionable assumptions about the velocity distribution (e.g., zero peculiar velocities of clumps in redshift space) into our distance estimates. In most places, as noted before, the bias is negligible. However, because the GA potential well has a broad minimum with a small velocity gradient, a systematic uncertainty of about ± 200 km s^{-1} in the velocities due to Malmquist bias translates into an uncertainty on the order of ± 500 km s^{-1} in the position of the center (e.g., 4200 km s^{-1} with the old weights and 5000 km s^{-1} with the new weights). Therefore we do not attempt to determine the distance to the center of the infall accurately at this stage.

The present analysis allows a closer look at our veteran—the Local Supercluster, centered on the Virgo cluster. The LSC shows up as an elongated ridge on the flank of the GA, extending along a line from Centaurus through Virgo toward Ursa Major (the line $Y \approx 1500$, $Z \approx 0$). Because of our large smoothing lengths, Virgo is only a minor bump on this elongated extension (Fig. 12). The flow in the LSC appears to be cylindrical, as noticed by Faber and Burstein (1988): an approximately cylindrically symmetric infall toward the line connecting Ursa Major and Virgo plus a stronger flow along this cylinder toward the GA. Virgo, when smoothed over a sphere of radius 1200 km s^{-1}, is moving with a velocity of 475 km s^{-1} almost precisely toward the center of the GA as defined by Faber and Burstein (1988).

Our Local Group lies at the outskirts of the extended ramp constituting the flank of the GA on the density contour $\delta\rho/\rho = 0.1 \pm 0.1$ (for $\Omega = 1$ and $R_w = 1200$ km s^{-1}, corresponding to $R_w \approx 1400$ km s^{-1} for the density). With 1200 km s^{-1} Gaussian smoothing, we find the velocity at the LG relative to the CMB to be 465 km s^{-1} in the direction $L = 157°$, $B = -17°$. This is roughly midway between the *unsmoothed* CMB dipole motion of the Local Group (620 km s^{-1} toward [136, −38]) and the average flow motion toward the center of the GA ($\sim$550 km s^{-1} toward [156, 9], where the direction comes from the potential minimum for $R_w = 1200$ km s^{-1}). As shown by Peebles (1988) and Faber and Burstein (1988), the Local Group and surrounding galaxies out to $\sim$700 km s^{-1} exhibit a "Local Anomaly" of $\sim$300 km s^{-1} with respect to the GA flow—the difference between the last two vectors above. Our smoothing scale of 1200 km s^{-1} evidently only partially resolves this anomaly.

On the opposite side of the sky from the GA and Virgo, in

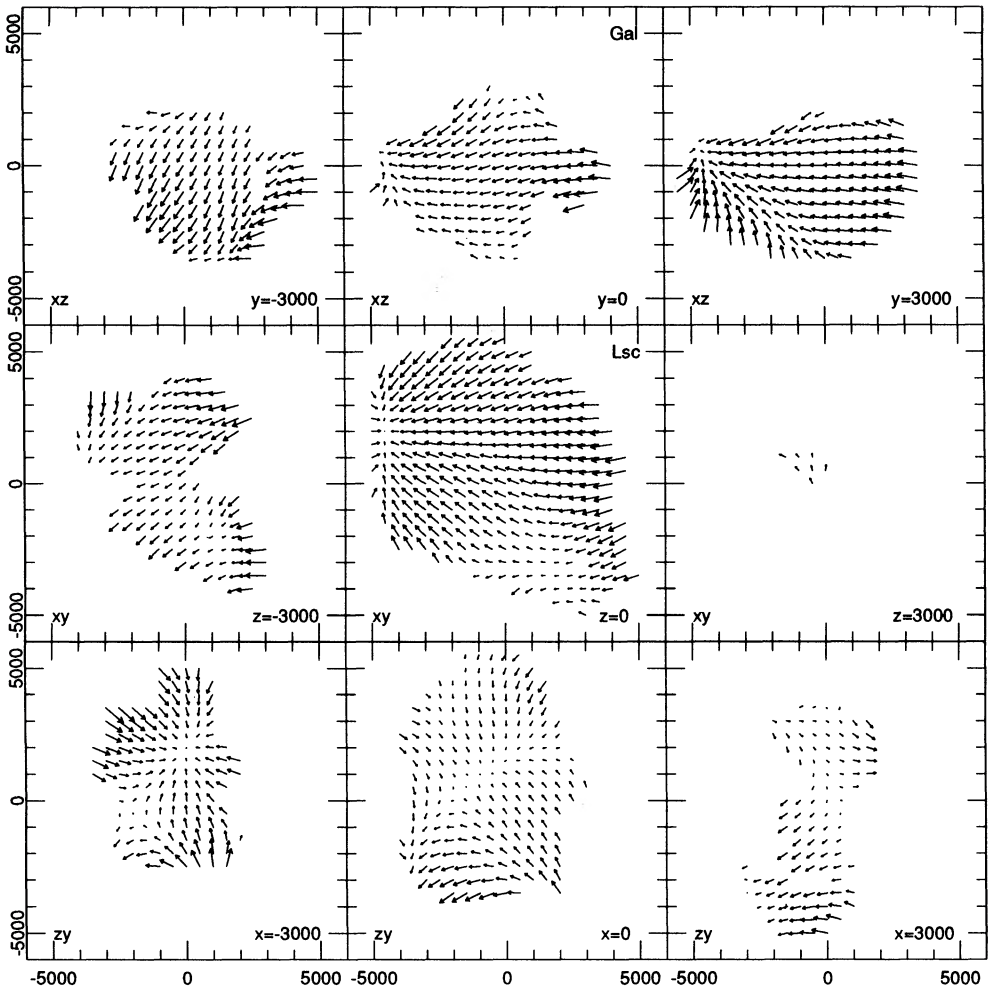

FIG. 6c

the south Galactic hemisphere at a distance of 2000 to 3000 km s^{-1} from the Local Group, is a large, elongated low-density region. Haynes and Giovanelli (1986) found a prominent void here in the foreground of the Perseus-Pisces supercluster, centered roughly at $X \approx 2500$, $Y \approx -2500$, $Z \approx 0$. Our most prominent low-density region is actually toward lower declination, at $X \lesssim 1000$, $Y \approx -3000$. There are voids here ($\alpha \approx 1^h$, $\delta \lesssim -10°$), too, in the Southern Sky Redshift Survey (da Costa *et al.* 1988). Void 1 of da Costa *et al.* is centered at $X \approx -1000$, $Y \approx -2700$, $Z \approx -900$, which coincides well with a low mass-density region found by POTENT. Our results suggest that there may be a low-density tube connecting the SSRS void with the Perseus-Pisces foreground void, roughly at a distance of 3000 km s^{-1} along the line $\alpha = 1^h$, $\delta \lesssim 20°$.

The most intriguing question raised by the present maps is: Where is the Perseus-Pisces supercluster? This being the second largest feature (after the GA) visible in the UGC and ESO catalogs, one might have expected POTENT to find a major density peak in its vicinity, i.e., at roughly the same distance as the GA but on the opposite side of the sky (at $X \approx 5000$, $Y \approx -1500$). (Perseus is at [348, −14], Pisces is at [328, 6], and Pegasus is at [298, 25].)

The *IRAS* redshift survey indeed shows the Perseus-Pisces supercluster to be as prominent as the GA (Yahil 1988). Our potential maps, however (LSC, Fig. 4) show only a weak potential valley leading from the Pisces region, passing south of the Local Group, and becoming lost in the GA potential well. Consistent with this, there is an indication of a weak cylindrical velocity flow toward Pisces (Fig. 6) and along this valley toward the GA. The only density peak that might plausibly be identified with the Perseus-Pisces chain in the Supergalactic plane is minor, lying south of Pisces ($X \approx 3000$, $Y \approx -3000$), closer to Pegasus than to Perseus (Fig. 9).

There are two aspects of the data used by POTENT that may cause us to underestimate the prominence of the Perseus-Pisces supercluster compared with redshift surveys. The first is the fact that the Perseus-Pisces region is severely undersampled (see Fig. 2). We noted before that sampling gradient bias distorts the velocity field in sparsely sampled regions. If one point, such as the Perseus cluster, has the dominant weight in a large volume—in fact, Figure 2 shows that it does—then the radial velocity field constructed with the tensor window function will be forced to be smooth in that region (see Fig. 3), with artificially small divergence and hence artificially diminished density perturbation. This is certainly a problem in the vicinity of the Perseus cluster (the isolated point with large weight at $X = 5700$, $Y = -1200$, $Z = -1500$ in Figs. 1 and 2).

The second point is that both the Perseus and Pisces clusters have significant motions toward the Local Group, and hence toward the GA. The radial peculiar velocity of Perseus in our

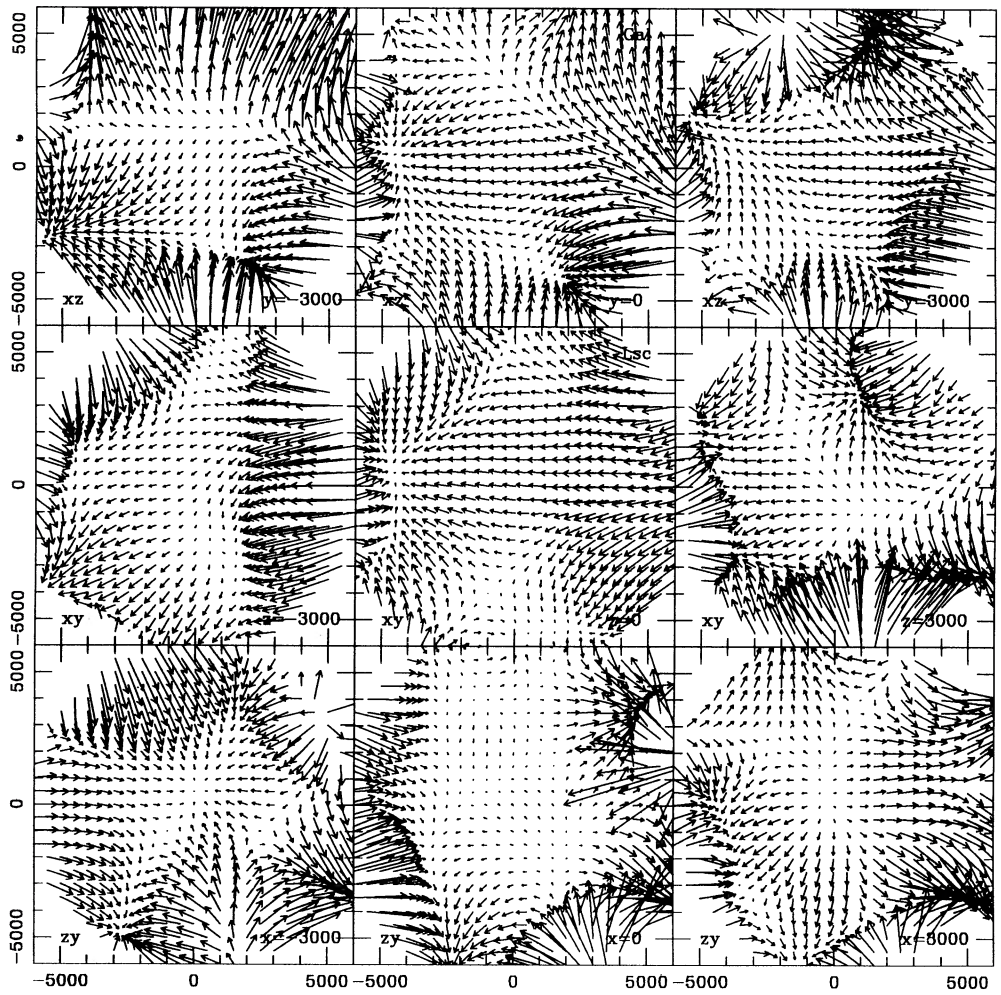

FIG. 7.—The velocity field, with W_F smoothing, in one Monte Carlo noise realization used to construct the error maps

sample is -814 km s^{-1}, and that of Pisces is -513 or -117 km s^{-1} (for the ellipticals and spirals, respectively). With such large motions toward the GA, the velocity potential is forced to be steadily declining from Perseus-Pisces toward the GA, with no potential minimum at Perseus-Pisces (Fig. 4). This effect would not be apparent with the gravitational potential determined purely from a redshift survey (such as *IRAS*) unless that survey was complete to distances much beyond Perseus-Pisces. Essentially, sampling problems affect POTENT and redshift surveys in opposite ways. Since the velocity potential at a given distance is determined by POTENT solely from the smoothed radial velocities interior to that distance, it is not affected by sparse sampling at larger distances. On the other hand, the gravitational potential and the velocities predicted from redshift surveys follow from integrating the mass distribution (deduced from the galaxy distribution) over all space, with the possibility that significant contributions are missed because of incompleteness at large distances. In contrast, redshift surveys reveal the density of galaxies without bias once sampling inefficiency is accounted for, while POTENT's recovery of the mass density, as we have seen, can be biased by local sparse sampling. The Perseus-Pisces region is a crucial target for more distance measurements and, indeed, there are several promising efforts in progress to measure distances to large numbers of spiral galaxies in this region (Freudling, Haynes, and Giovanelli 1989; Courteau and Faber 1989; Willick 1990).

Besides missing Perseus-Pisces, the density maps show a mysterious strong density peak at $X \approx 2500$, $Y \approx -2000$, $Z \approx -3500$. The maximum density (with an effective Gaussian smoothing radius of 1400 km s^{-1}) is as large as the GA, although this structure occupies less volume than the GA. The mystery peak is at about the same distance as Pisces but is 50° away on the sky and does not seem to coincide with any known, visible supercluster. The peak results from data on Abell 400, which has a negative radial peculiar velocity, plus 10 elliptical galaxies, mostly in the NGC 1600 and NGC 1700 groups, which consistently show high positive peculiar velocities of several hundred km s^{-1} and were highlighted as anomalous by Lynden-Bell *et al.* (1988). However, in the current sample this region is practically empty otherwise (see Fig. 2 and the sparseness cut of Fig. 6*c*) and may be subject to sampling gradient bias arising from the strong weight given to the spiral cluster Abell 400. This region deserves close attention in future surveys.

Finally, we make a brief comparison of our reconstructed maps with the simulated maps of DBF for an unbiased cold dark matter (CDM) N-body simulation. The simulation was

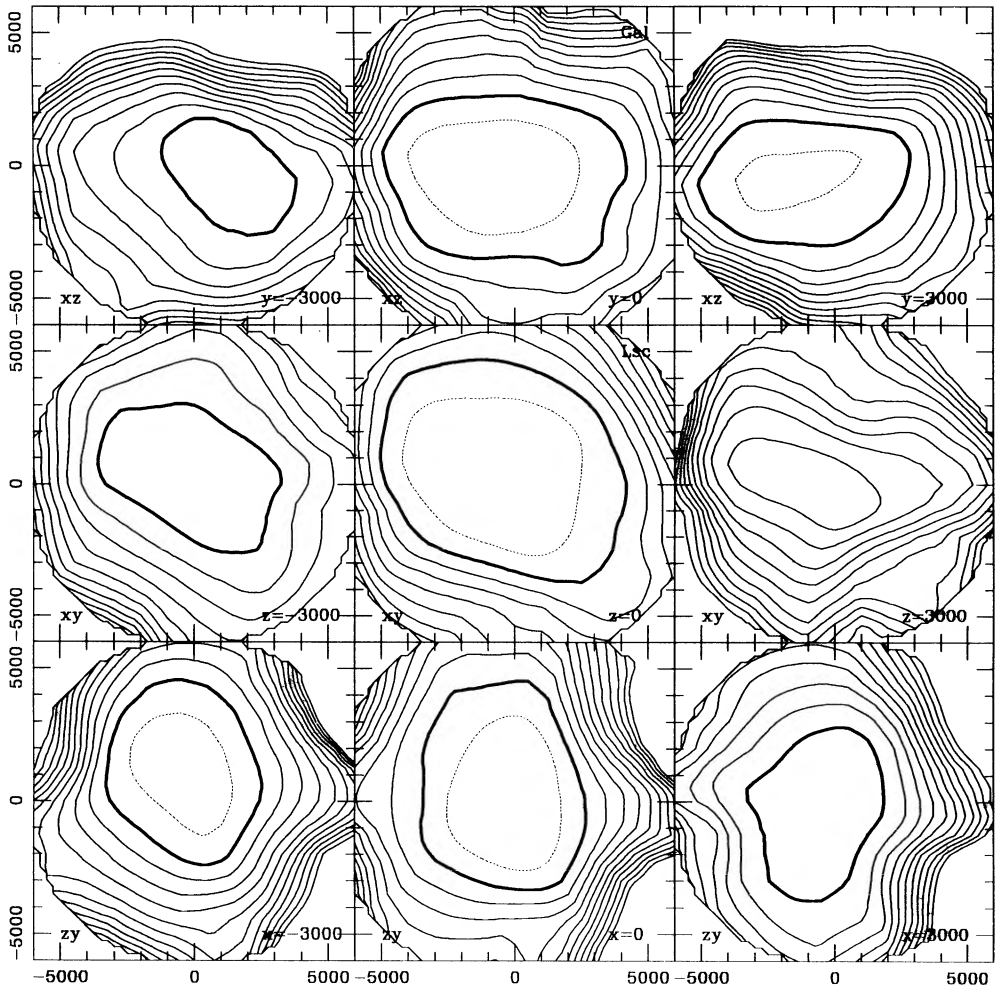

FIG. 8.—Standard error in the three-dimensional velocity field with W_F (corresponding to Fig. 6*b*), obtained from 100 Monte Carlo noise simulations. Contour spacing is 100 km s^{-1}, with the heavy contour at 300 km s^{-1} and the dotted contour at 200 km s^{-1}.

sampled using the same sparse "mask" of positions and errors as the data, and random distance errors were added to the N-body peculiar velocities and redshifts as described by DBF. The unbiased amplitude was selected by DBF so as to give large streaming velocities (relative to a biased model) for the purpose of testing POTENT, not for testing the CDM theory. We stress that this is not a rigorous test of the CDM theory, since we did not simulate exactly the observational procedure with the N-body simulation (e.g., we did not apply the selection function to the scattered distances nor did we apply a Malmquist correction). Even more importantly, a definitive test of a stochastic theory cannot be made using only one random sample. However, this comparison raises issues that we will address in a later, more systematic test of theories.

The typical scale size of features in the potential and velocity maps shown above is comparable to the size of structures appearing in the noisy CDM reconstructions (DBF, Figs. 8 and 10). However, the *amplitude* of the observed flows in the real data is nearly twice as large as in the simulation, even though the "Local Group" in the simulation has a peculiar velocity of ~ 500 km s^{-1}. The amplitude problem is seen most clearly by comparing the potential fields: the data maps (Fig. 4 of this paper) have about twice as many contours as the simulation maps (Fig. 10 of DBF). A comparable problem is apparent with the density (note that the density contour spacing is 0.2 in $\delta\rho/\rho$ in this paper but 0.1 in DBF). The discrepancy between the real universe and this realization of the CDM model is comparable to that estimated for CDM by Bertschinger and Juszkiewicz (1988) using the simple flow models of Faber and Burstein (1988) to represent the large-scale velocity field. It is noteworthy that this discrepancy shows up even for the unbiased version of the CDM model.

VI. FURTHER APPLICATIONS

The maps presented above provide a useful way to visualize the results of POTENT. However, their construction is only the initial step of an extended program of *a priori* statistical analysis of the recovered dynamical fields for comparison with the galaxy distribution and with theoretical models. Here we present a few preliminary results of an ongoing analysis program.

Given the high density of distance measurements within 3000 km s^{-1} from the Local Group, together with the success of POTENT in reconstructing the velocity and density fields even in moderately nonlinear regions, we have constructed higher resolution maps of the nearby flows. Figure 14 shows the reconstructed density and velocity fields in the Supergalactic plane using a fixed window of Gaussian smoothing

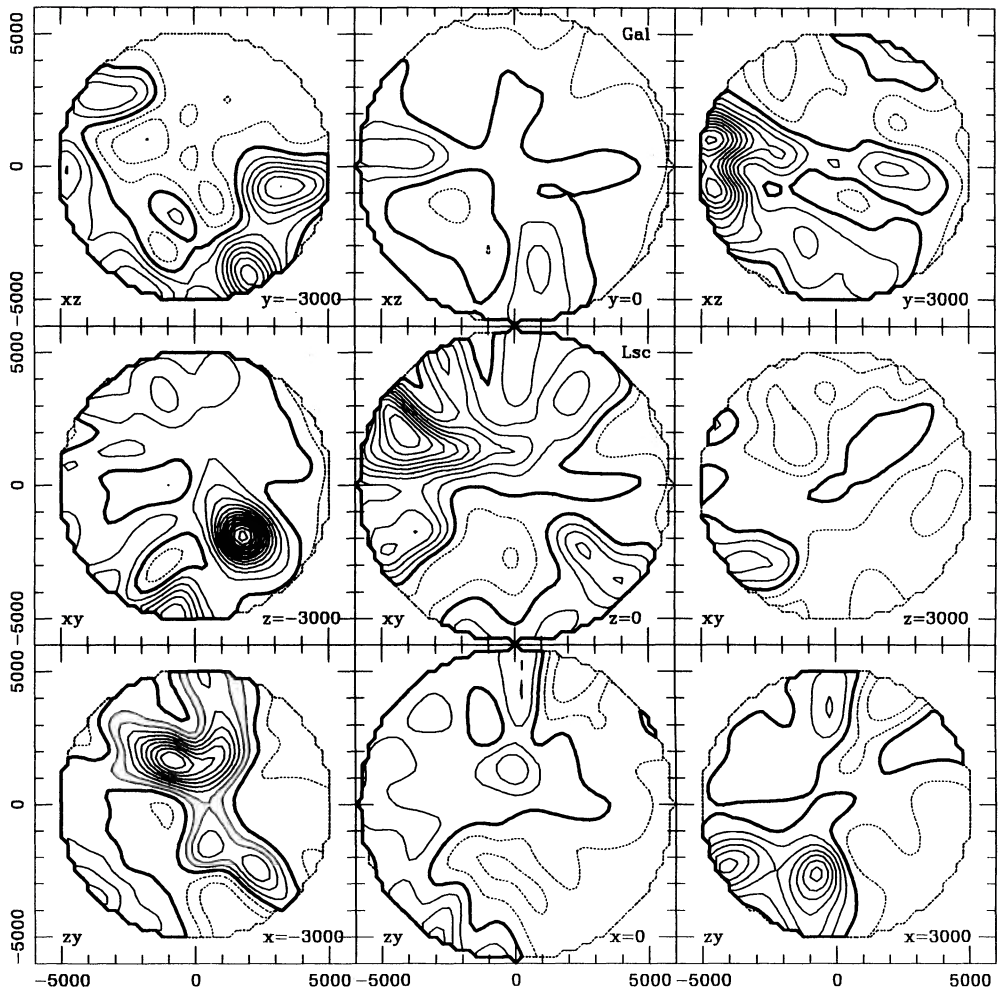

FIG. 9*a*

FIG. 9.—Reconstructed density contrast field $\delta\rho/\rho$. Contour spacing is 0.2, with positive contours solid, negative contours dotted and the zero contour heavy. $\Omega = 1$ has been assumed to convert peculiar velocities to the displacements needed for the density reconstruction; a smaller Ω would lead to a larger amplitude of density fluctuations ($\delta\rho/\rho \propto \Omega^{-0.6}$ for small amplitudes). (*a*) W_V. (*b*) W_F.

radius $R_w = 500$ km s^{-1} (effectively $\approx$700 km s^{-1} for the density). Comparison of this map with Plate 15 of the *Nearby Galaxies Atlas* (Tully and Fisher 1987) reveals an encouraging correlation between the distributions of light and mass. A quantitative comparison awaits further tests of POTENT's accuracy on such small scales using N-body simulations.

The high-resolution velocity field in the linear approximation can be used to estimate the relative gravitational influence of Virgo and the GA on the Local Group. Figure 15 shows the peculiar velocities in the CMB frame, smoothed with a Gaussian of fixed radius 500 km s^{-1}, at the positions of Virgo and the LG. The total smoothed velocity at the LG is 565 ± 125 km s^{-1} (with Monte Carlo standard errors of the three-dimensional velocity) in the direction $L = 147°$, $B = -23°$. The component of this velocity in the direction of the GA (using the Faber-Burstein center at $L = 161°$, $B = -6°$) is 522 km s^{-1}. Thus the smoothed velocity at the LG is directed mostly toward the GA. The velocity at Virgo is 658 ± 121 km s^{-1} and is directed almost precisely toward the GA. The residual velocity at the LG normal to the direction to the GA is 215 km s^{-1}. This residual vector actually points $\sim$45° away from Virgo toward Ursa Major and $\sim$45° below the Supergalactic plane; its component toward Virgo itself is only 123 km s^{-1}. This does not prove that only 20% of the Local Group velocity is caused by Virgo, since we can trade off motions toward Virgo and the GA, but, the fact that Virgo has a large peculiar velocity directed toward the GA suggests that the dominant source of the motion of both the Local Group and Virgo is the GA. Note that the projection of the Local Group CMB dipole velocity in the direction of Virgo ($L = 103°$, $B = -2°$) is 420 km s^{-1}.

Table 2 summarizes the velocity measurements centered on the Local Group. Note that the standard errors of V refer to the magnitude of the velocity, i.e., they are one-dimensional errors, in contrast with the three-dimensional errors quoted above. The velocity vectors shows a nice progression in direction from the smallest scale outward to the main flow toward the GA (the 500 km s^{-1} top-hat window being effectively smaller than the 500 km s^{-1} Gaussian because of the extended wings of the Gaussian). The average velocities within 4000 and 6000 km s^{-1} were computed using the three-dimensional velocity field from POTENT with 1200 km s^{-1} Gaussian smoothing, so that the effective top-hat radii are increased slightly to $\sim$4300 and 6400 km s^{-1}.

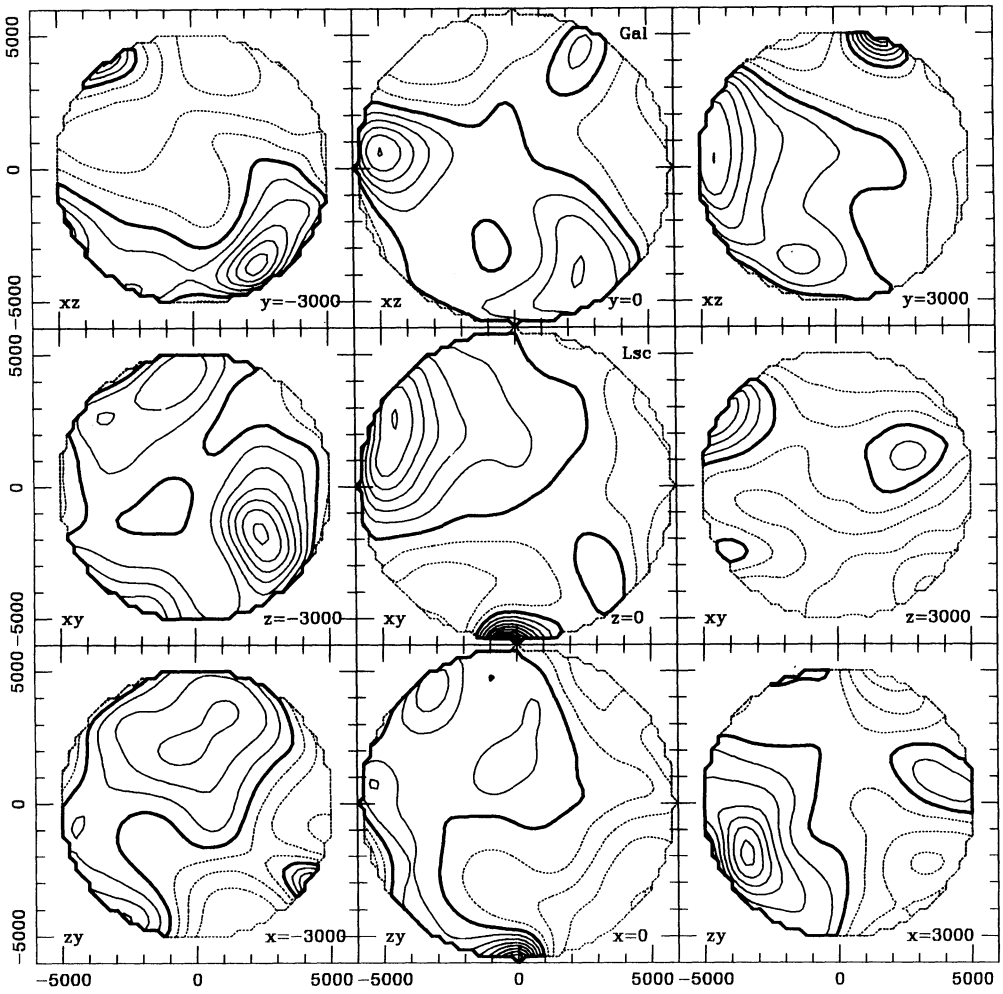

FIG. 9*b*

The volume-weighted velocity within 6000 km s^{-1}, 327 ± 82 km s^{-1}, is significantly smaller than the 599 ± 104 km s^{-1} computed by Dressler *et al.* (1987*b*) using a maximum-likelihood bulk flow solution for the elliptical galaxies out to 6000 km s^{-1} distance. Unlike the previous bulk flow solutions, our determination suffers little from the shrinkage of the effective window due to the tapering with distance of the sample selection function and the inverse variance weighting of individual measurements (Kaiser 1988) or from the use of only radial velocities (Regős and Szalay 1989). Even though these limitations of the data are present in the input to POTENT, we first compute a *local* three-dimensional velocity field that is not biased as much as the *global* bulk flow. (First, the volume weighting within each smoothing window tends to eliminate the sampling gradient bias. Second, although the measurements from the inner parts of each window are still weighted higher because of the inverse variance weighting, this effect is limited to relatively small distances on the order of the smoothing radius.) Then, integrating the velocity with uniform volume weighting (we did not use inverse variance weighting for this volume integration), we obtain a bulk flow estimate for a meaningful spherical scalar window function. For comparison, the rms velocity predicted by the cold dark matter model (Davis *et al.* 1985) for a randomly placed observer with a combination of 1200 km s^{-1} Gaussian and 6000 km s^{-1} top-hat spherical smoothing is 224 σ_ρ km s^{-1}, where σ_ρ is the rms relative mass fluctuation in a sphere of radius 800 km s^{-1}, serving here as an uncertain normalization factor. (For an "unbiased" model, $\sigma_\rho = 1$, while for the linear bias model with bias factor 2.5, $\sigma_\rho = 0.4$.) For the 4000 km s^{-1} top-hat with additional 1200 km s^{-1} Gaussian smoothing, the CDM predicted rms velocity is 287 σ_ρ km s^{-1}, compared with the measurement of 388 ± 67 km s^{-1}. The error bars include only the effects of random distance errors, but not the effect of sampling

TABLE 2

SPHERICALLY AVERAGED VELOCITY AT THE LOCAL GROUP

Velocity or Window	V (km s^{-1})	L	B
CMB Dipole[a]	620 ± 30	136	−38
500 km s^{-1} top-hat[b]	623 ± 89	142	−33
500 km s^{-1} Gaussian	577 ± 63	144 ± 5	−15 ± 10
1200 km s^{-1} Gaussian	457 ± 61	156 ± 7	−19 ± 12
General flow toward GA	550 ± 150	156[c]	9[c]
4000 km s^{-1} top hat[d]	388 ± 67	177 ± 9	−15 ± 17
6000 km s^{-1} top hat[d]	327 ± 82	194 ± 13	5 ± 26

[a] From Lubin *et al.* 1985 with heliocentric to LG conversion of 300 km s^{-1} toward $l = 90°$, $b = 0$.

[b] From Faber and Burstein 1988.

[c] Direction to the velocity potential minimum.

[d] With additional smoothing by 1200 km s^{-1} Gaussian.

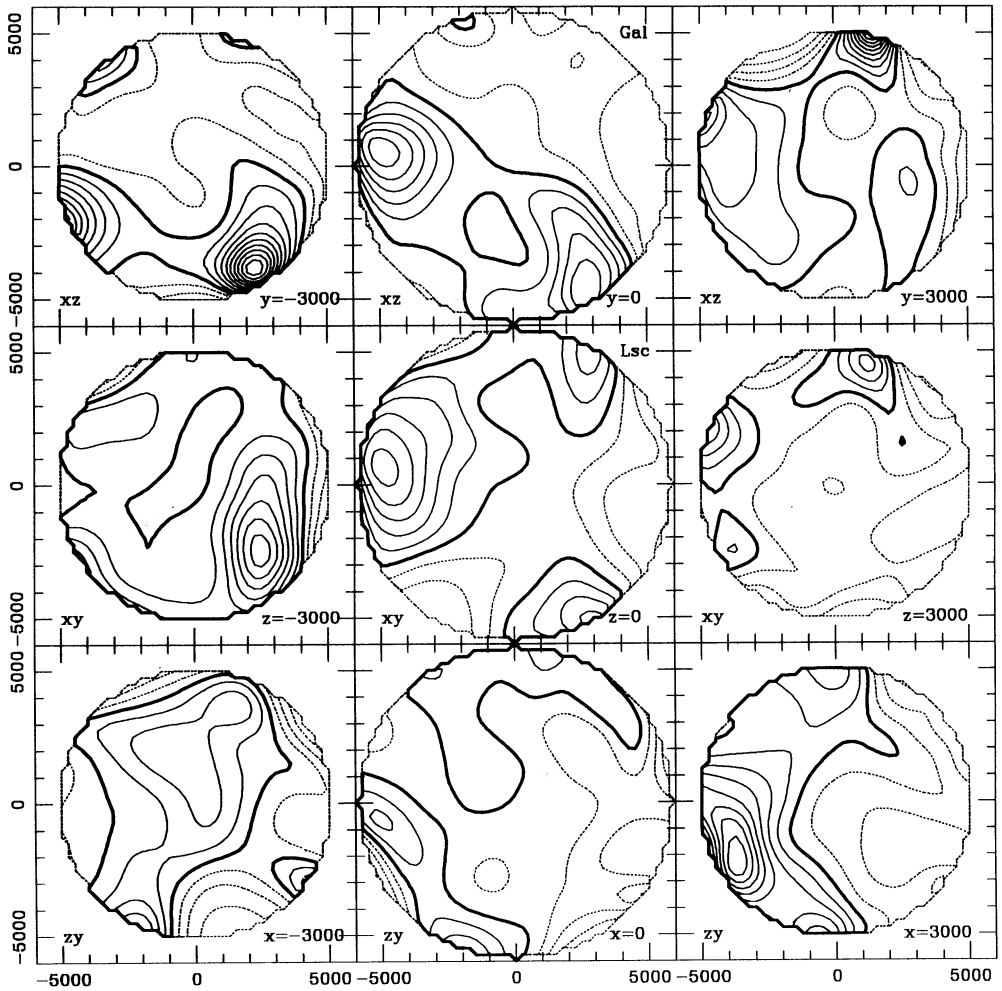

FIG. 10.—The density contrast field, with W_F smoothing, in one Monte Carlo noise realization. Contours as in Fig. 9.

gradient bias, which is dependent on the underlying velocity field and is difficult to estimate. We have less confidence in the velocity within 6000 km s^{-1} than in the velocities on smaller scales because large volumes are unsampled within the 6000 km s^{-1} radius sphere. We have not yet tried to place confidence levels on the success or failure of the cold dark matter model in this comparison, but it appears that the model fares better in this large-scale bulk flow test than one might have originally thought. We caution that more extensive comparisons are needed to test the CDM theory, especially since we noted above that *typical* observed velocities are too small by nearly a factor of 2 compared with one N-body realization of the CDM model.

Figure 16 shows the Supergalactic components of the bulk flow velocity $\boldsymbol{V}(R)$ averaged over a sphere of radius R centered on the LG, computed as described above for $R = 4000$ and 6000 km s^{-1}. The error bars are standard errors computed, as usual, from Monte Carlo noise simulations. Since we have used the velocity field over the entire volume for this calculation, including the poorly sampled regions, the true errors may be larger because of sampling gradient bias which becomes increasingly severe for $R > 4000$ km s^{-1}.

Note that $\boldsymbol{V}(R)$ is not expected to be proportional to the cumulative flux dipole shown, e.g., by Strauss and Davis (1988) and Yahil (1988) from the *IRAS* redshift survey or by Lynden-Bell, Lahav, and Burstein (1989) from optical catalogs, since the cumulative dipoles relate directly only to $\boldsymbol{V}(0)$. However, we can make an approximate comparison with these dipoles, too. The velocities in Table 2 may be compared with the optical dipole $\boldsymbol{D}$ of Lynden-Bell *et al.*, with top-hat smoothing radii of 500, 1000, and 2000 km s^{-1}, $(D, L, B) = (600, 147, -38)$, (499, 160, −36), and (306, 174, −36), respectively. (The normalization of the optical dipole, D, has been arbitrarily set to 600 km s^{-1} for the 500 km s^{-1} sphere.) In linear theory, if light traces mass, $\boldsymbol{D}(R)$ is the contribution to the peculiar velocity of the Local Group from matter beyond radius R. This is similar (but not exactly equal) to the peculiar velocity averaged over a sphere of radius R centered at the origin, which is listed in Table 2. The approximate agreement between the mean velocity from POTENT and the optical dipole seems to indicate a general similarity between the light distribution and the mass distribution within ~2000 km s^{-1}. We are pursuing several other methods for comparing the results of POTENT with the results from the *IRAS* redshift survey and from optical catalogs in order to investigate how well mass traces light on large scales.

A novel application of the reconstructed potential field is to make a prediction of the anisotropy of the cosmic microwave background radiation (CMB) induced by large-scale gravitational potential gradients. Bertschinger, Górski, and Dekel

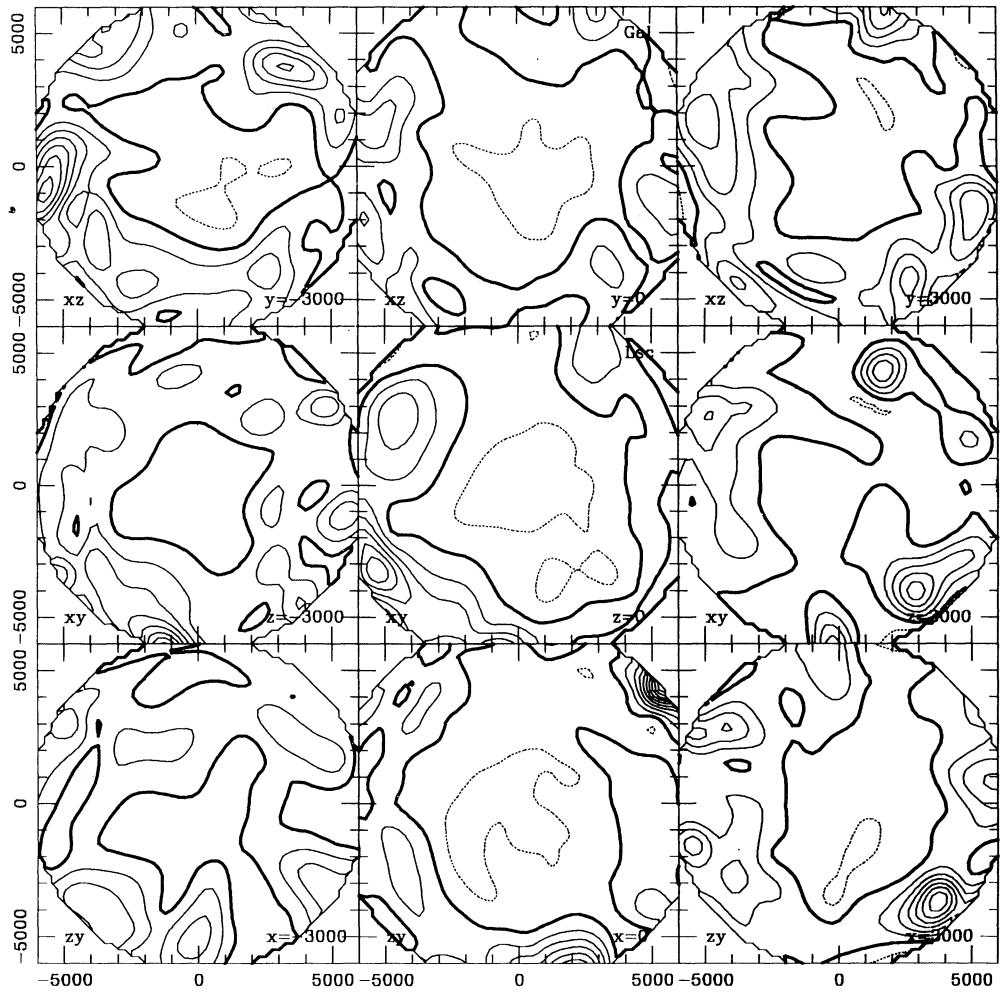

FIG. 11.—Standard error in the density contrast field with W_F (corresponding to Fig. 9*b*), obtained from 20 Monte Carlo noise simulations. Contour spacing is 0.1, with the heavy contour at 0.2 and the dotted contour at 0.1.

(1990) have made maps of the CMB anisotropy $\Delta T/T$ that would be seen by a distant observer, nearly at the edge of our horizon, who sees the last scattering of the CMB photons as they are climbing out of the potential well of the GA and surrounding regions. The differential gravitational redshift (Sachs and Wolfe 1967) across the Supergalactic plane leads to a maximum $\Delta T/T \approx 2 \times 10^{-5}$ on a scale of one degree if $\Omega = 1$. If $\Omega < 1$ the anisotropy has larger amplitude and occurs at a smaller angular separation. Note that this anisotropy is caused by nearby potential wells but is seen only by a very distant observer; local observers would see a negligible imprint of the GA on the CMB. However, if the universe is statistically homogeneous on large scales we would expect to see anisotropy of similar magnitude on similar angular scales, caused by the progenitors of GA–like structures present in the last-scattering surface.

VII. DISCUSSION

We have processed the local universe through a cosmic "CAT scan," converting one-dimensional peculiar velocities into a three-dimensional picture using the fact that gravity produces potential flows. This technique has not only allowed us to restore the missing tangential components of the velocity field, it has also enabled us to reconstruct the three-dimensional mass density distribution. No assumptions have been made concerning how mass traces light. Instead, we have assumed that galaxies and other test bodies fall freely in the large-scale gravitational field. Because the gravitational field is the gradient of a scalar potential, one component of the velocity field is sufficient to restore all three components. To reconstruct the density we also assumed that the smoothed density perturbations are not too large in amplitude, so that a quasi-linear approximation is valid. Our density values are measured relative to the cosmological mean density and we need to assume a value of Ω to get $\delta\rho/\rho$. Fortunately, we are completely insensitive to the uncertain value of the Hubble constant.

The theoretical ideas behind POTENT are fairly obvious in hindsight and are straightforward to implement. Bertschinger and Dekel (1989) first applied the method to ideal data from an N-body simulation, with perfect sampling and no distance errors. The reconstruction was much better than we had hoped, encouraging us to apply the technique to real data. The real universe of sparse galaxy samples with frustratingly large relative distance errors has presented a much greater challenge. After a great deal of effort to design and test optimal methods for handling sparse and noisy redshift-distance samples, described in detail by Dekel, Bertschinger, and Faber (1990),

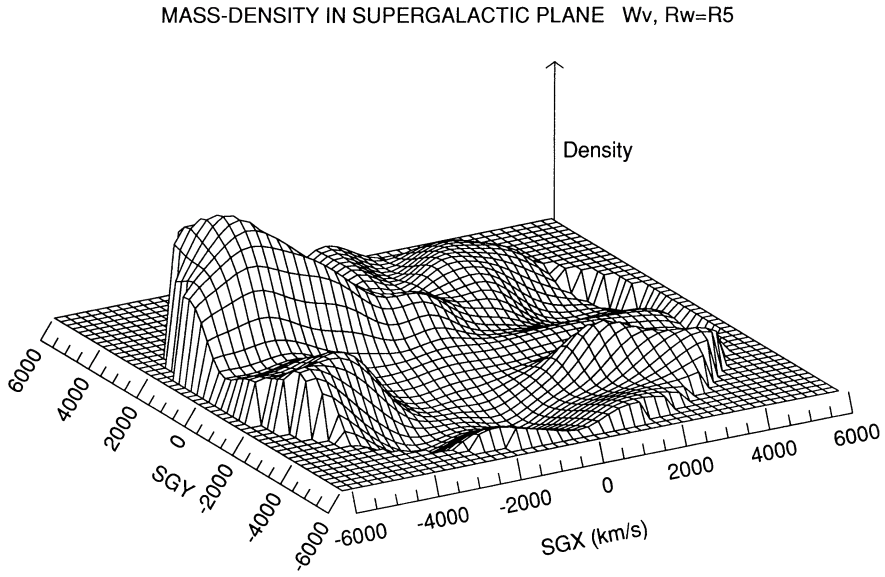

FIG. 12*a*

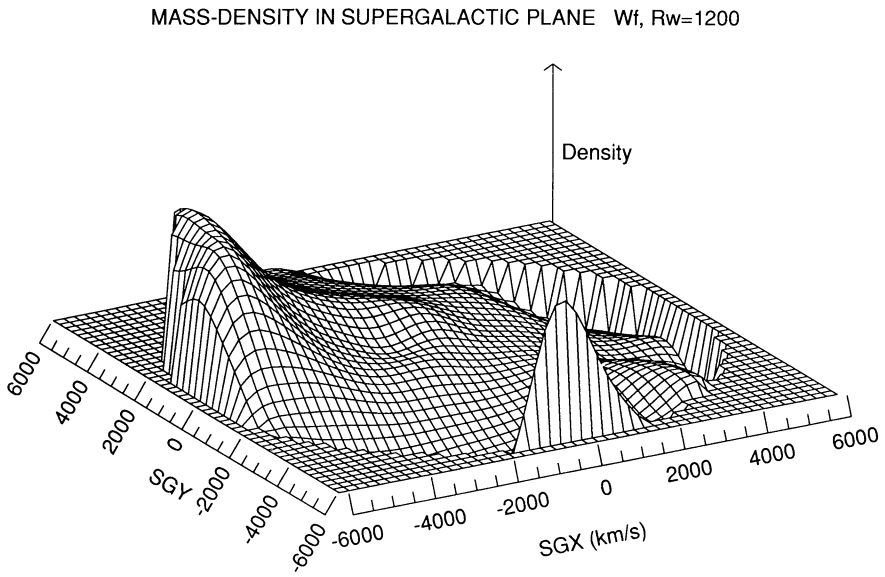

FIG. 12*b*

FIG. 12.—The reconstructed mass density field in the Supergalactic plane (same as central panel of Fig. 9). (*a*) W_V. (*b*) W_F.

we finally trust the method enough to present here the first results of application to the real universe.

Given our assumptions, the scalar velocity potential, the velocity field, and the mass density field all provide a complete description of the dynamics, since each contains enough information to reconstruct the others. However, we have found that all three together provide a useful and complementary set of maps. The main product of this paper is this set of maps, given in Figures 4, 6, and 9. Because the measurement errors are not small, we provide a corresponding set of standard error maps (Figs. 5, 8, and 11), plus some noisy versions of our maps extracted from the Monte Carlo simulations that are the heart of our error analysis. We have found it a challenge to present three-dimensional scalar and vector fields containing lots of structure in a way that enables one to form a picture of the dynamics without sacrificing too much detail. The plots of nine slices through a sphere are a relatively crude representation that we expect to improve in the future.

Our maps contain many features, and we prefer not to reduce them to one or two objects described by a handful of parameters, since the signal-to-noise ratio is sufficient to provide much more detail. However, there is one dominant large-scale feature that is apparent in all our maps, as it was to Lynden-Bell *et al.* (1988): the great attractor in the southern celestial hemisphere, with which the Hydra-Centaurus supercluster is associated. The GA is most apparent in the maps of velocity potential (roughly proportional to the gravitational potential) because it is so large in extent. It dominates the dynamics across a region more than 6000 km s^{-1} in diameter. The density peak of the GA is located approximately at $L = 156°$, $B = 9°$, with maximum $\delta\rho/\rho = 1.2 \pm 0.4$ for $\Omega = 1$ with smoothing by a Gaussian filter of effective radius ≈ 1400

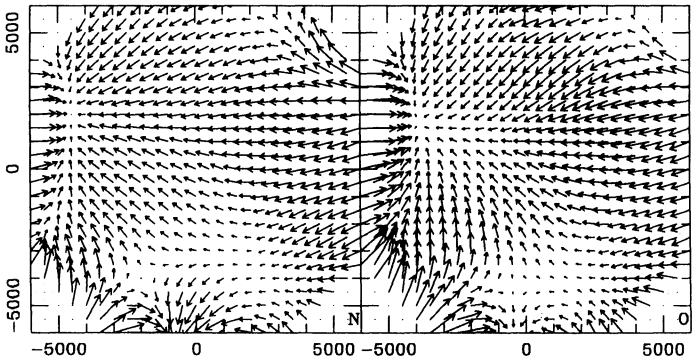

FIG. 13.—The reconstructed velocity field in the Supergalactic plane using different σ_i weights in the smoothing procedure. Left: σ_i is a constant fraction of the estimated distance, as in the rest of this paper, plus $\sigma_f = 150$ km s^{-1} added in quadrature. Right: σ_i is a constant fraction of the distance as estimated by the redshift in the LG frame.

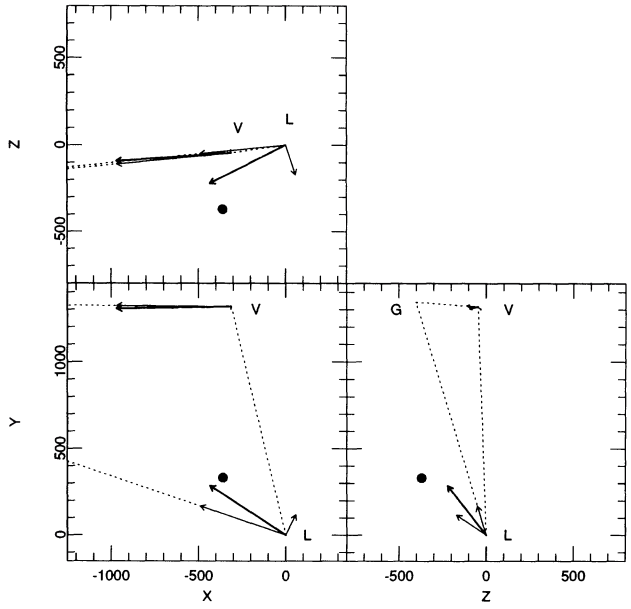

FIG. 15.—Reconstructed velocities at the Local Group (L) and the Virgo cluster (V), smoothed over 500 km s^{-1} in the CMB frame. The filled circle marks the (unsmoothed) LG velocity relative to the CMB based on the temperature dipole. The dotted lines mark the directions to the GA as defined by Faber and Burstein. The Local Group velocity is decomposed into components parallel and perpendicular to the direction of the GA.

km s^{-1}. This is at the same Supergalactic longitude as the Centaurus clusters but is 20° higher in latitude, closer to the Supergalactic plane but on the opposite side. With a Gaussian smoothing radius of 1200 km s^{-1}, we determine the velocities at the Local Group and Virgo to be 465 and 475 km s^{-1}, respectively, with three-dimensional standard errors of about 100 km s^{-1}. Both velocities are directed closely toward the GA; the Virgo velocity is almost perpendicular to our line of sight to Virgo.

The distance to the minimum of the GA potential is slightly more uncertain than had been previously realized and depends on the exact weights applied in defining the smooth velocity field. Random distance errors and possible residual Malmquist bias arising from density gradients along the line of sight prevent us from locating the center to better than ± 500 km s^{-1}. The true distance probably lies somewhere between 4200 and 5200 km s^{-1}, the extremes given by the different weighting methods. There is some evidence in the data for infall from the back side of the GA, but the signal is only about one standard deviation based on our Monte Carlo noise simulations (see also Dressler and Faber 1990*a*, *b* and Burstein *et al.* 1990).

The Local Supercluster, including the Virgo and Ursa Major clusters, appears to be an elongated extension of the GA. Even with a smoothing scale as little as 500 km s^{-1}, the smoothed mass density evaluated at the position of the Virgo cluster seems to be smaller than the smoothed mass density at the Centaurus clusters in the foreground of the GA (Fig. 14).

The Perseus-Pisces supercluster does not live up to one's expectations, dynamically speaking, based on its prominence in galaxy catalogs. We see very little sign of it except for a minor density peak associated with Pisces. However, poor sampling in this region leads to a sampling gradient bias in our method that may cause us to underestimate the magnitude of the density perturbations there: the Perseus cluster has large weight over a large volume, so that POTENT fits a nearly uniform velocity field over this region, with artificially reduced divergence and suppressed density. There is little that can be done about this short of acquiring more data, although we can estimate the magnitude of the error from Monte Carlo simulations based on N-body simulations with known velocity and density fields. The same problem exists in the Galactic plane

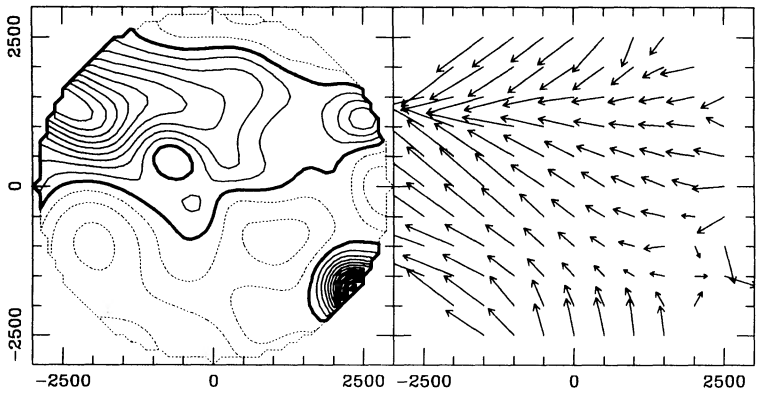

FIG. 14.—A high-resolution view of the density and velocity fields in the Supergalactic plane within 3000 km s^{-1}. Fixed smoothing window, $R_w = 500$ km s^{-1}. Contours are the same as in Fig. 9.

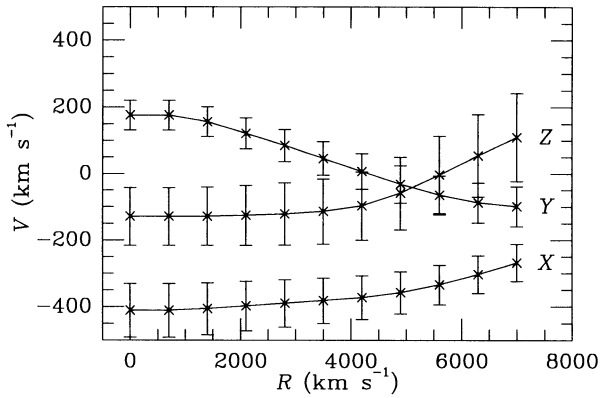

FIG. 16.—The velocity averaged over a sphere of radius R centered on the Local Group, computed from the $R_w = 1200$ km s^{-1} fixed-window velocity field reconstruction. Equal weight has been given to equal volumes. Error bars are from 20 Monte Carlo noise simulations.

between Centaurus and Pavo, where it is likely that we underestimate the strength of the bridge between these clusters. At present we are at least able to identify these regions based on the sampling density. Figure 6*c* shows how much of the volume within 6000 km s^{-1} has a trustworthy velocity reconstruction, based on Monte Carlo errors combined with the sampling density criterion. Our conservative view is that we must wait for more data in the Perseus-Pisces region before concluding that there is a discrepancy between the large-scale peculiar velocity field and the galaxy distribution.

POTENT seems to do well in picking out nearby voids in the galaxy distribution as being underdense in mass. The large low-density region in our large-scale maps (Fig. 9) coincides roughly with the void in front of the Perseus-Pisces chain (Haynes and Giovanelli 1986) and extending to the south (da Costa *et al.* 1988, void 1). Nearby voids in the Supergalactic plane (Tully and Fisher 1987) show up in our high-resolution density maps (Fig. 14).

Our qualitative global impression is of similarity between the mass density distribution as deduced from POTENT and the galaxy distribution, despite the discrepancies in some regions such as Perseus-Pisces. This rough agreement is encouraging for standard theories of cosmological structure formation, which predict a correlation of mass and light, although perhaps with some bias.

Our results essentially confirm the basic picture of Lynden-Bell *et al.* (1988), based on their modeling of the raw radial velocities. However, by obtaining a three-dimensional, model-independent view of the structure, we can refine the details and present the local cosmography in a more visually comprehensible form and in a form more appropriate for theoretical analysis using *a priori* statistics. Most importantly, the use of POTENT gives the cosmographical results a physical basis: apart from the limitations of imperfect data, these are the dynamical fields underlying the observed radial velocities if the structure has evolved by *gravity*.

It is possible that the distance measurements at the heart of our analysis suffer from some undetected systematic errors that might masquerade as peculiar velocities. For example, Silk (1989) and Djorgovski *et al.* (1989) have suggested that mass-to-light ratios may vary with environment so as to shift the zero-points of the $D_n - \sigma$ and IRTF relations. However, tests of environment-dependent systematic effects have been carried out by Dressler and Faber (1990*a*, *b*) and Burstein *et al.* (1990), with negative results. Moreover, it is difficult to imagine a physical mechanism that could generate the required coherence of a spurious flow across such a large volume containing a large range of environmental conditions. Such a mechanism might well be theoretically more problematic than the large scale motions. Nevertheless, the possibility of systematic errors must be investigated thoroughly.

It is difficult to test for systematic errors in the distance estimates using peculiar velocities alone. However, the similarity in the velocity fields recovered from spirals and E/S0s (Faber and Burstein 1988; Dressler and Faber 1990*a*, *b*; Burstein *et al.* 1990; present paper), based on two different measurement techniques, suggests that systematic errors are not important. Additional support comes from a study of the $L_x - L_{opt}$ relation, which is found to be tighter for ellipticals when $D_n - \sigma$ distances are used (Donnelly *et al.* 1990). If our preliminary indications for similarity between the mass and light distributions are confirmed, this will provide yet another positive argument for the reality of the velocities. This similarity is also evidence for potential flow—our basic assumption that is otherwise only theoretically motivated and cannot be tested directly.

The potential, velocity, and density fields we have reconstructed have many important applications that we plan to address in future work. One of the major goals is to deduce the initial conditions for the formation of structure in our universe, allowing us to test theories such as the cold dark matter model and the inflationary universe paradigm. The density and potential fields on large scales should, according to theory, reflect the initial conditions and hence they provide a direct test of the theories, bypassing the problematic issue of galaxy formation. Since observations of large-scale motions appear to present difficulties for some theoretical models, it is important to recognize also that observations can guide us independently of particular theoretical models.

A second major goal of POTENT is to understand how luminous galaxies trace the underlying mass distribution in the universe. Mass and light clearly do not trace each other exactly, but the extent to which the galaxy distribution is biased with respect to the mass distribution is highly uncertain because of our unsatisfactory understanding of galaxy and star formation. Yet, this bias is one of the key ingredients of theories such as the "standard" biased cold dark matter model (Kaiser 1984; Davis *et al.* 1985; Dekel and Rees 1987), and it plays a major role in the effort to determine the value of the cosmological density parameter Ω. Unfortunately, the absolute degree of bias is coupled inextricably with the unknown value of Ω, at least in linear theory. Nevertheless, a scaled map of the large-scale, mass-to-light ratio would be helpful. At least it should be possible to determine whether a given biasing model (e.g., the linear biasing of Gaussian density peaks [Kaiser 1984]) is rejected by the data. We are pursuing comparisons with several different galaxy catalogs.

The results presented here and in DBF are encouraging given the present imperfect state of the data, but they are just the beginning of a long-term project. The sparseness of present samples, combined with significant scatter in the distance indicator relations, is the current major source of error. With additional data we expect a gradual improvement in the quality of our results. A comparison of the resolution in various parts of the volume obtained with the fixed-radius smoothing window and the varying window (Fig. 6) shows where we currently have the best data and where more data are required (see also

Fig. 2). The Perseus-Pisces region is an obvious case where data are urgently needed. Other poorly sampled regions are in the constellations Libra-Corona Borealis and Dorado-Phoenix-Tucana and regions of Galactic latitude $b \lesssim 20°$. The near future promises new data for spirals, S0s and ellipticals that will fill in some of the poorly sampled regions and will allow us to probe larger volumes. POTENT can deal with heterogeneous new data sets as soon as they become available. We encourage observers to continue this important work.

E. B. and S. M. F. acknowledge the hospitality of the Hebrew University, E. B. and A. Dekel acknowledge the hospitality of U.C. Santa Cruz, and A. Dekel acknowledges the hospitality of M.I.T. We thank G. R. Blumenthal, W. G. Mathews, J. R. Primack, and M. Strauss for stimulating discussions. E. B. thanks the John von Neumann Center for their grant of supercomputer time used for the N-body simulations. This research has been supported by NASA Astrophysics Theory grant NAGW-1320, by NSF grants PHY88-00801 and AST90-01762, by NSF grants PHY82-17853 and AST87-02899 supplemented by funds from NASA, by the US-Israel Binational Science Foundation grant 86-00190, and by the Israeli Academy Basic Research grant 316/87.

REFERENCES

Aaronson, M., *et al.* 1989, *Ap. J.*, **338**, 654 (A89).
Aaronson, M., Bothun, G., Mould, J., Huchra, J., Schommer, R. A., and Cornell, M. E. 1986, *Ap. J.*, **302**, 536 (A86).
Aaronson, M., Huchra, J., and Mould, J. 1979, *Ap. J.*, **229**, 1.
Aaronson, M., *et al.* 1982*a*, *Ap. J. Suppl.*, **50**, 241 (A82).
Aaronson, M., Huchra, J., Mould, J., Schechter, P. L., and Tully, R. B. 1982*b*, *Ap. J.*, **258**, 64.
Bertschinger, E., and Dekel, A. 1989, *Ap. J.* (*Letters*), **336**, L5 (BD).
———. 1990, in *Large-Scale Structure and Peculiar Motions in the Universe*, ed. D. W. Latham and L. N. da Costa (San Francisco: Astronomical Society of the Pacific), in press (BD90).
Bertschinger, E., Górski, K. M., and Dekel, A. 1990, *Nature*, **345**, 507.
Bertschinger, E., and Juszkiewicz, R. 1988, *Ap. J.* (*Letters*), **334**, L59.
Bothun, G. D., Aaronson, M., Schommer, B., Huchra, J., and Mould, J. 1984, *Ap. J.*, **278**, 475 (B84).
Burstein, D. 1990, *Rept. Progr. Phys.*, in press.
Burstein, D., Faber, S. M., and Dressler, A. 1990, *Ap. J.*, **354**, 18.
Collins, C. A., Joseph, R. D., and Robertson, N. A. 1986, *Nature*, **320**, 506.
Courteau, S., and Faber, S. M. 1989, in *The Extragalactic Distance Scale*, ed. S. van den Bergh and C. J. Pritchet (Provo: Astronomical Society of the Pacific), p. 366.
da Costa, L. N., *et al.* 1988, *Ap. J.*, **327**, 544.
Davis, M., Efstathiou, G., Frenk, C. S., and White, S. D. M. 1985, *Ap. J.*, **292**, 371.
Davis, M., and Peebles, P. J. E. 1983, *Ann. Rev. Astr. Ap.*, **21**, 109.
Dekel, A., and Bertschinger, E. 1990, in *Large-Scale Structure and Peculiar Motions in the Universe*, ed. D. W. Latham and L. N. da Costa (San Francisco: Astronomical Society of the Pacific), in press (DB90).
Dekel, A., Bertschinger, E., and Faber, S. M. 1990, *Ap. J.*, **364**, 349 (DBF).
Dekel, A., and Rees, M. J. 1987, *Nature*, **326**, 455.
de Vaucouleurs, G., and Peters, W. L. 1984, *Ap. J.*, **287**, 1.
de Vaucouleurs, G., de Vaucouleurs, A., and Corwin, H. 1976, *Second Reference Catalogue of Bright Galaxies* (Austin: University of Texas).
Djorgovski, S., and Davis, M. 1987, *Ap. J.*, **313**, 59.
Djorgovski, S., de Carvalho, R. and Han, M.-S. 1989, in *The Extragalactic Distance Scale*, ed. S. van den Bergh and C. J. Pritchet (Provo: Astronomical Society of the Pacific), p. 329.
Donnelly, R. H., Faber, S. M., and O'Connell, R. M. 1990, *Ap. J.*, **354**, 52.
Dressler, A. 1987, *Ap. J.*, **317**, 1.
———. 1988, *Ap. J.*, **329**, 519.
Dressler, A., and Faber, S. M. 1990*a*, *Ap. J.*, **354**, 17.
———. M. 1990*b*, *Ap. J.* (*Letters*), **354**, L45.
Dressler, A., Lynden-Bell, D., Burstein, D., Davies, R. L., Faber, S. M., Terlevich, and Wegner, G. 1987*a*, *Ap. J.*, **313**, 42.
Dressler, A., Faber, S. M., Burstein, D., Davies, R. L., Lynden-Bell, D., Terlevich, and Wegner, G. 1987*b*, *Ap. J.* (*Letters*), **313**, L37.
Faber, S. M., and Burstein, D. 1988, in *Large-Scale Motions in the Universe*, ed. V. C. Rubin and G. V. Coyne (Princeton: Princeton University Press), p. 115.
Faber, S. M., Wegner, G., Burstein, D., Davies, R. L., Dressler, A., Lynden-Bell, D., and Terlevich, R. J. 1989, *Ap. J. Suppl.*, **69**, 763.
Fall, S. M., and Jones, B. J. T. 1976, *Nature*, **262**, 457.
Freudling, W., Haynes, M. P., and Giovanelli, R. 1989, in *The Extragalactic Distance Scale*, ed. S. van den Bergh and C. J. Pritchet (Provo: Astronomical Society of the Pacific), p. 361.
Górski, K., Davis, M., Strauss, M. A., White, S. D. M., and Yahil, A. 1989, *Ap. J.*, **344**, 1.
Górski, K., Hoffman, Y., and Bertschinger, E. 1990, in preparation.
Groth, E. J., Juszkiewicz, R., and Ostriker, J. P. 1989, *Ap. J.*, **346**, 558.
Hart, L., and Davies, R. D. 1982, *Nature*, **297**, 191.
Haynes, M. P., and Giovanelli, R. 1986, *Ap. J.* (*Letters*), **306**, L55.
Kaiser, N. 1984, *Ap. J.* (*Letters*), **284**, L9.
———. 1988, *M.N.R.A.S.*, **231**, 149.
———. 1989, in *Large-Scale Structure and Motions in the Universe*, ed. M. Mezzetti, G. Giuricin, F. Mardirossian, and M. Ramella (Dordrecht: Kluwer), p. 197.
Lightman, A., and Schechter, P. L. 1990, preprint.
Lilje, P. B., Yahil, A., and Jones, B. J. T. 1986, *Ap. J.*, **307**, 91.
Lubin, P., Villela, T., Epstein, G., and Smoot, G. 1985, *Ap. J.* (*Letters*), **298**, L1.
Lucey, J. R., and Carter, D. 1988, *M.N.R.A.S.*, **235**, 1177.
Lynden-Bell, D., Faber, S. M., Burstein, D., Davies, R. L., Dressler, A., Terlevich, R. J., and Wegner, G. 1988, *Ap. J.*, **326**, 19 (7S).
Lynden-Bell, D., Lahav, O., and Burstein, D. 1989, *M.N.R.A.S.*, **241**, 325.
Ostriker, J. P., and Suto, S. 1990, *Ap. J.*, **348**, 378.
Peebles, P. J. E. 1980, *The Large-Scale Structure of the Universe* (Princeton: Princeton University Press).
———. 1988, *Ap. J.*, **332**, 17.
Regős, E., and Szalay, A. S. 1989, *Ap. J.*, **345**, 627.
Rubin, V. C., Thonnard, N., and Ford, W. K., Jr. 1976, *A.J.*, **81**, 719.
Sachs, R. K., and Wolfe, A. M. 1967, *Ap. J.*, **147**, 73.
Shaya, E. J. 1984, *Ap. J.*, **280**, 470.
Silk, J. 1989, *Ap. J.* (*Letters*), **345**, L1.
Strauss, M., and Davis, M. 1988, in *Large-Scale Motions in the Universe*, ed. V. C. Rubin and G. V. Coyne (Princeton: Princeton University Press), p. 255.
Tammann, G. A., and Sandage, A. 1985, *Ap. J.*, **294**, 81.
Tully, R. B., and Fisher, J. R. 1977, *Astr. Ap.*, **54**, 661.
———. 1987, *Nearby Galaxies Atlas* (Cambridge: Cambridge University Press).
Vittorio, N., and Turner, M. S. 1987, *Ap. J.*, **316**, 475.
Willick, J. A. 1990, *Ap. J.* (*Letters*), **351**, L5.
Yahil, A. 1988, in *Large-Scale Motions in the Universe*, ed. V. C. Rubin and G. V. Coyne (Princeton: Princeton University Press), p. 219.
Zel'dovich, Ya. B. 1970, *Astr. Ap.*, **5**, 84.

EDMUND BERTSCHINGER: Department of Physics, MIT, 6-207, Cambridge, MA 02139

DAVID BURSTEIN: Department of Physics, Arizona State University, Tempe, AZ 85721

AVISHAI DEKEL: Racah Institute of Physics, The Hebrew University of Jerusalem, Jerusalem 91904, Israel

ALAN DRESSLER: The Observatories of the Carnegie Institution of Washington, 813 Santa Barbara Street, Pasadena, CA 91101

SANDRA FABER: UCO/Lick Observatory, University of California, Santa Cruz, CA 95064